ABSTRACT

Title of dissertation: TWO-DIMENSIONAL TURBULENCE WITH DRAG

Yue-Kin Tsang, Doctor of Philosophy, 2004

Dissertation directed by: Professor Edward Ott
Department of Physics

We consider the enstrophy cascade in forced two-dimensional turbulence with a linear drag force. In the presence of linear drag, the energy wavenumber spectrum drops with a power law faster than in the case without drag, and the vorticity field becomes intermittent, as shown by the anomalous scaling of the vorticity structure functions. Using a previous theory, we compare numerical simulation results with predictions for the power law exponent of the energy wavenumber spectrum and the scaling exponents of the vorticity structure functions ζ_{2q} obtained in terms of the distribution of finite time Lyapunov exponents. We also study, both by numerical experiment and theoretical analysis, the multifractal structure of the viscous enstrophy dissipation in terms of its Rényi dimension spectrum D_q and singularity spectrum $f(\alpha)$. We derive a relation between D_q and ζ_{2q}, and discuss its relevance to a version of the refined similarity hypothesis. In addition, we obtain and compare theoretically and numerically derived results for the dependence on separation r of the probability distribution of $\delta_{\vec{r}}\omega$, the difference between the vorticity at two points separated by a distance r. Our numerical simulations are done on a 4096×4096 grid.

TWO-DIMENSIONAL TURBULENCE WITH DRAG

by

Yue-Kin Tsang

Dissertation submitted to the Faculty of the Graduate School of the
University of Maryland, College Park in partial fulfillment
of the requirements for the degree of
Doctor of Philosophy
2004

Advisory Commmittee:

Professor Edward Ott, Chair/Advisor
Professor Thomas M. Antonsen,Jr.
Dr. Parvez N. Guzdar

ACKNOWLEDGMENTS

I would like to thank my advisor Professor Edward Ott for his guidance and support. Over the past five years, he has provided me with invaluable insights and constant encouragement. He has also given me, with his infinite patience, the freedom to explore the challenging field of fluid turbulence. It is a great pleasure for me to be able to learn from one of the most outstanding scholars in the field of nonlinear science.

I am also grateful to Professor Thomas M. Antonsen, Jr., who has always dazzled me with his brilliant ideas and sparkling humor. He has always made himself available for help and advice. My numerous discussions with him were extremely enlightening.

I wish to express my deepest appreciation to Dr. Parvez N. Guzdar. This thesis would not have been completed without his extraordinary computational expertise. I owe a great debt of gratitude to him for all the numerical skills he has taught me.

Thanks are also due to Professor Daniel P. Lathrop and Professor Brian R. Hunt for agreeing to serve on my thesis committee and their careful perusal of the manuscript. I have really enjoyed the stimulating discussions with Professor Lathrop.

Finally, I would like to acknowledge the financial support from the Office of Naval Research and the National Science Foundation (PHYS 0098632).

TABLE OF CONTENTS

LIST OF TABLES

LIST OF FIGURES

Chapter 1 Introduction

Two-dimensional Navier-Stokes turbulence has attracted much interest because of its relevance to a variety of natural flow phenomena. Examples are plasma in the equatorial ionosphere [1] and the large-scale dynamics of the Earth's atmosphere and oceans [2]. In the laboratory, experiments that are close to two-dimensional, such as soap film flow [3, 4] and magnetically forced stratified flow [5], have been conducted. In addition, rotating fluid systems [6] are used to study quasi-two-dimensional turbulence and its relevance to large-scale planetary flow. Ref. [7] gives a review of some recent experiments in two-dimensional turbulence.

In many of the situations involving two-dimensional turbulence, there are regimes where drag is an important physical effect. In the ionospheric case, there is drag friction of the plasma as it moves relative to the neutral gas background (due to ion-neutral collision). For geophysical flows and rotating fluid experiments, viscosity and the no-slip boundary condition give rise to Ekman friction. In this case the three-dimensional flow is often modeled as two-dimensional outside the layer adjoining the no-slip boundary, and the effect of the boundary layer manifests itself as drag in the two-dimensional description. For soap film and magnetically forced flows, friction is exerted on the fluids by surrounding gas and the bottom of the container, respectively. In all these cases, the drag force can be modeled as proportional to the two-dimensional fluid velocity $\vec{v}$, thus the describing Navier-Stokes momentum equation becomes,

$$\frac{\partial \vec{v}}{\partial t} + (\vec{v} \cdot \nabla)\vec{v} = -\frac{1}{\rho}\nabla p + \nu \nabla^2 \vec{v} - \mu \vec{v} + \vec{f}\,, \tag{1.1}$$

where ρ is the fluid density, μ is the drag coefficient, ν is the kinematic viscosity and $\vec{f}$ is an external forcing term. In two-dimensions, the system can be described by the scalar vorticity field ω whose equation of motion is obtained by taking the curl of Eq. (1.1),

$$\frac{\partial \omega}{\partial t} + \vec{v} \cdot \nabla \omega = \nu \nabla^2 \omega - \mu \omega + f_\omega \tag{1.2}$$

with $\omega = \hat{z} \cdot \nabla \times \vec{v}$ and $f_\omega = \hat{z} \cdot \nabla \times \vec{f}$, $\hat{z}$ being the unit vector perpendicular to the plane. In our studies, the forcing will be taken to be localized at small wavenumbers (k) with a characteristic wavenumber k_f, and incompressibility, $\nabla \cdot \vec{v} = 0$, will be assumed.

According to Kraichnan, for two-dimensional turbulence with no drag and very small viscosity, for $k \gg k_f$, up to the viscous cutoff k_d, enstrophy cascades from small to large k [8]. As a result, the energy wavenumber spectrum $E(k)$ has a power law behavior with logarithmic correction [9], $E(k) \sim k^{-3}[\ln(k/k_f)]^{-1/3}$ for $k_f \ll k \ll k_d$. In the presence of a linear drag, the energy spectrum drops with a power law faster than the case with no drag [11, 10],

$$E(k) \sim k^{-(3+\xi)} \qquad (\xi > 0) \ , \tag{1.3}$$

and there is no logarithmic correction.

Furthermore, the vorticity field is intermittent, as indicated by the anomalous scaling of the vorticity structure functions [11, 12, 13]. The structure function of order $2q$, $S_{2q}(\vec{r})$ is defined as the $(2q)^{\text{th}}$ moment of the absolute value of the vorticity difference $\delta_{\vec{r}}\omega = \omega(\vec{x}+\vec{r}) - \omega(\vec{x})$. Assuming that the system is homogeneous and isotropic, the structure functions depend on $r = |\vec{r}|$ only. For the case with drag ($\mu > 0$), it is found that, in the enstrophy cascade range ($k_d^{-1} \ll r \ll k_f^{-1}$), $S_{2q}(r)$ scales with r as,

$$S_{2q}(r) = \langle |\delta_{\vec{r}}\omega|^{2q} \rangle \sim r^{\zeta_{2q}} \tag{1.4}$$

with $\zeta_{2q} > 0$. Furthermore, the vorticity structure functions show anomalous scaling; that is, ζ_{2q} is a nonlinear function of q. The nonlinear dependence of ζ_{2q} on q indicates that the vorticity field is intermittent. In contrast, in the absence of drag ($\mu = 0$), it is predicted [5] that $\omega(\vec{x})$ wiggles rapidly (*i.e.*, on the scale k_d^{-1}) and homogeneously in space. In terms of Eq. (1.4), this corresponds to $\zeta_{2q} = 0$ for $\mu = 0$.

The intermittency of the vorticity field also manifests itself as a change in shape or form of the probability distribution function of the vorticity difference $\delta_{\vec{r}}\omega$ with the separating distance r. It can be shown that if the probability distribution function $\bar{P}_r(X_{\vec{r}})$ of the standardized vorticity difference,

$$X_{\vec{r}} = \frac{\delta_{\vec{r}}\omega}{\sqrt{\langle (\delta_{\vec{r}}\omega)^2 \rangle}} \ , \tag{1.5}$$

is independent of r, then ζ_{2q} increases linearly with q: From Eq. (1.4) and Eq. (1.5),

$$S_{2q}(r) = \langle |\delta_{\vec{r}}\omega|^2 \rangle^q \int |X_{\vec{r}}|^{2q} \bar{P}_r(X_{\vec{r}}) \, dX_{\vec{r}} \ , \tag{1.6}$$

and, if $\bar{P}_r(X_{\vec{r}})$ is independent of r, for r in the cascade range, then the only r-dependence of $S_{2q}(r)$ comes through the term $\langle|\delta_{\vec{r}}\omega|^2\rangle^q$, implying $\zeta_{2q} = q\zeta_2$; that is, ζ_{2q} is linearly proportional to q. Such collapse of $\bar{P}_r(X_{\vec{r}})$ for different values of r has been observed in an experiment [5] where drag is believed to be unimportant. When the effect of drag is not negligible, we find that $\bar{P}_r(X_{\vec{r}})$ changes shape and develops exponential or stretched-exponential tails as r decreases, so that Eq. (1.6) admits nonlinear dependence of ζ_{2q} on q.

The intermittency of the vorticity field is closely related to the multifractal structure of the viscous enstrophy dissipation field. We define the enstrophy as $\omega^2/2$. From Eq. (1.2), the time evolution of the enstrophy is then given by

$$\begin{aligned}\frac{\partial}{\partial t}\left(\frac{\omega^2}{2}\right) &= -\nabla\cdot\left[\vec{v}\left(\frac{\omega^2}{2}\right) - \nu\nabla\left(\frac{\omega^2}{2}\right)\right] - \nu|\nabla\omega|^2 \\ &\quad -2\mu\left(\frac{\omega^2}{2}\right) + \omega f_\omega \ . \end{aligned} \tag{1.7}$$

We identify the second term on the right hand side of Eq. (1.7) as the local rate of viscous enstrophy dissipation η,

$$\eta = \nu|\nabla\omega|^2 \ . \tag{1.8}$$

The multifractality of the viscous enstrophy dissipation can be quantified by the Rényi dimension spectrum of a measure based on the vorticity gradient. Imagine we divide the region $\mathcal{R}$ occupied by the fluid into a grid of square boxes of size ϵ, we define the measure p_i of the i^{th} box $\mathcal{R}_i(\epsilon)$ as

$$p_i(\epsilon) = \frac{\int_{\mathcal{R}_i(\epsilon)}|\nabla\omega|^2\,d\vec{x}}{\int_{\mathcal{R}}|\nabla\omega|^2\,d\vec{x}} \ . \tag{1.9}$$

The Rényi dimensions spectrum [14] based on this measure is then given by,

$$D_q = \frac{1}{q-1}\lim_{\epsilon\to 0}\lim_{\nu\to 0}\frac{\log\sum_i p_i^q}{\log\epsilon} \ . \tag{1.10}$$

The definition Eq. (1.10) was introduced in the context of natural measures occurring in dynamical systems by Grassberger [15], and Hentschel and Procaccia [16]. In the case with drag, we find that the dimension spectrum for p_i is multifractal, that is D_q varies with q, in contrast to the case with no drag in which $D_q = 2$, indicating that the measure is uniformly rough.

The measure p_i can also be described in terms of the singularity spectrum $f(\alpha)$ [17]. In particular, to each box $\mathcal{R}_i$, we associate a singularity index α_i via

$$\alpha_i = \frac{\log p_i}{\log \epsilon} \ , \tag{1.11}$$

and the number of boxes $N(\alpha)d\alpha$ with singularity index between α and $\alpha + d\alpha$ is then assumed to scale as

$$N(\alpha) \sim \epsilon^{-f(\alpha)} \ . \tag{1.12}$$

$f(\alpha)$ can loosely be interpreted as the dimension of the set of boxes with singularity index α [18]. When $f(\alpha)$ and D_q are smooth functions, $f(\alpha)$ is related to D_q by a Legendre transformation [17]. The multifractal nature of the viscous enstrophy dissipation in the presence of drag implies that the $f(\alpha)$ spectrum, defined by Eq. (1.11) and Eq. (1.12), is a nontrivial function of α.

The subject of this dissertation is the relation of $\bar{P}_r(X_{\vec{r}})$, the exponents, ξ and ζ_{2q}, and the fractal dimension D_q to the chaotic properties of the turbulent flow. In chaotic flows, the infinitesimal separation between two fluid particle trajectories, $\delta\vec{x}(t)$ typically diverges exponentially. The net rate of exponentiation over a time interval from 0 to t for a trajectory starting at $\vec{x}_0$ is given by the finite-time Lyapunov exponent, h defined as,

$$h(t;\vec{x}_0) = \frac{1}{t}\log\frac{|\delta\vec{x}(t)|}{|\delta\vec{x}(0)|} \, . \tag{1.13}$$

At a particular time t, $h(t;\vec{x}_0)$ in general depends on the initial positions $\vec{x}_0$ and the initial orientation of the perturbation $\delta\vec{x}(0)$. However, for large t, the results for $h(t;\vec{x}_0)$ is insensitive to the orientation of $\delta\vec{x}(0)$ for typical choices of $\delta\vec{x}(0)$, and we neglect the dependence on $\delta\vec{x}(0)$ in what follows. The distribution in the values of h for randomly chosen $\vec{x}_0$ can be characterized by the conditional probability density function $P(h\,|\,t)$. In subsequent chapters, we shall review the theories that relate ξ [11] and ζ_{2q} [19] to the distribution $P(h\,|\,t)$ and the drag coefficient μ. We then derive an expression for $\bar{P}_r(X_{\vec{r}})$ and a relation between D_q and ζ_{2q}. We apply these theories to compute ξ, ζ_{2q}, $\bar{P}_r(X_{\vec{r}})$ and D_q for turbulent flows governed by Eq. (1.2) and the theoretical results are compared to those obtained from direct numerical simulations.

We perform our simulations on a square domain of size $[-\pi,\pi]\times[-\pi,\pi]$ with periodic

boundary conditions in both directions. The viscous term in Eq. (1.2) is replaced by a hyperviscous damping $-\nu\nabla^8\omega$ with $\nu = 7.5 \times 10^{-25}$ and $f_\omega(x, y) = \cos 2x$ is used for the source function of the vorticity. Our use of a hyperviscosity is similar to what is often done in numerical studies of three-dimensional turbulence and, for a given numerical resolution, has the desirable effect of increasing the scaling range where dissipation can be neglected, while, at the same time it is hoped that this change in the dissipation does not influence the scaling range physics. For wavenumber $k \leq 6$, we have $\mu = 0.1$ and this provides an energy sink at the large scales. For $k > 6$, we will consider the cases of $\mu = 0.1$ and $\mu = 0.2$. As we shall see in Chapter 2, when drag is present, the large k vorticity components can be considered as being passively advected by the small k flow components. Applying the same small k drag (*i.e.*, μ=0.1 for $k \leq 6$) allows us to compare the effects of drag at small scales while keeping similar large scale dynamics of the flows. For all the numerical results presented here, we use a spatial grid of 4096×4096 and the time step equals 0.00025. Starting from random initial conditions for the vorticity field, Eq. (1.2) is integrated using a time split-step method described in detail in Ref. [20]. The system appears to reach a statistical steady-state after about 40 time units. FIG. 1.1 shows snapshots of the vorticity field for the cases of $\mu(k > 6) = 0.1$ and $\mu(k > 6) = 0.2$. We note that the vorticity field for the case with a larger drag shows less fine structure and the large scale vortices tend to have shorter lifetime. At any given moment, there are typically 3 – 5 large vortex structures visible in the system. In the steady-state, vortices are continuously created and destroyed.

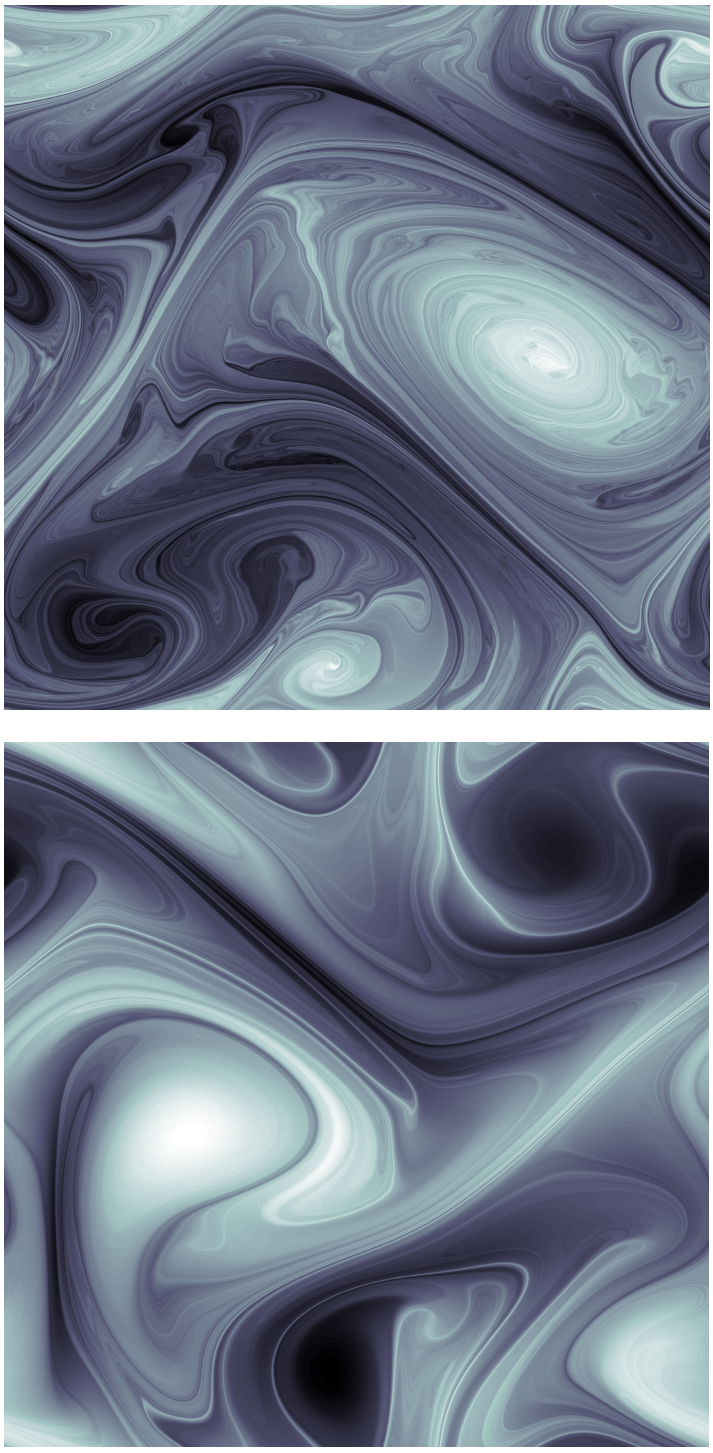

Figure 1.1: Snapshots of the vorticity field $\omega(x, y)$ at $t = 61$ for the case $\mu(k > 6) = 0.1$ (upper) and at $t = 65$ for the case $\mu(k > 6) = 0.2$ (lower) ($\mu = 0.1$ for $k \leq 6$ for both cases). Light areas are regions of large positive values of the vorticity, and dark areas are regions of negative vorticity of large magnitude. The scales used in the two plots are not the same.

Chapter 2 Wave-packet Model and the Distribution of Lyapunov Exponent

The theory that we will use is based on the approximation that the high k components of the vorticity field are passively advected by the large scale structures of the flow. This can be justified by the following argument given in Ref [11]. The Lyapunov exponent h of the flow is the mean rate of exponentiation of differential displacement $\delta\vec{x}$ following the flow, where $d(\delta\vec{x})/dt = \delta\vec{x}\cdot\nabla\vec{v}$. Thus one can crudely estimate the Lyapunov exponent as

$$h \sim \langle \|\nabla\vec{v}\|^2 \rangle^{\frac{1}{2}} \sim \sqrt{\int_{k_f}^{\infty} k^2 E(k) dk} \ , \tag{2.1}$$

where $\|\nabla\vec{v}\|^2 = (\partial v_x/\partial x)^2 + (\partial v_y/\partial y)^2 + (\partial v_x/\partial y)^2 + (\partial v_y/\partial x)^2$. Assuming the limit of infinite Reynolds number and power law behavior of $E(k)$ valid as $k \to \infty$, the integral in Eq. (2.1) diverges at the upper limit unless ξ in Eq. (1.3) is positive. That is, the velocity field $\vec{v}$ is not differentiable (h and $\nabla\vec{v}$ are undefined) unless $\xi > 0$ (alternatively, if $\xi < 0$ and viscosity imposes a cutoff to power law behavior of $E(k)$ at $k \sim k_d$, then, although $\|\nabla\vec{v}\|^2$ is now finite, the integral in Eq. (2.1) is dominated by velocity components at the shortest wavelength). From Eq. (2.1), for $\xi > 0$, we have $h \sim k_f^{-\xi/2}$. This means that h, which characterizes small scale stretching, is determined by the largest scale flow components. Since $\xi > 0$ in the case where drag is present, $\nabla\vec{v}$ is determined by the largest spatial scales. Thus the Lyapunov exponents provide information on the evolution of the distance between fluid elements whose separation is *finite* but small compared to k_f^{-1}. This will allow us to approximate the evolution of vorticity field components with wavenumbers in the range $k_f \ll k < k_d$ using Lyapunov exponents that result primarily from the large spatial scales $k \sim k_f$. That is, the vorticity field at wavenumber $k_f \ll k < k_d$ evolves via approximately passive advection by the large scale flow. (Note that for $\xi < 0$ such an approach would not be applicable since the Lyapunov numbers would provide an estimate of separation evolution only for distances less that k_d^{-1} which is outside the dissipationless power law range.)

Note that the case without drag corresponds to $\xi = 0$, which is marginal in the sense that it is on the borderline of the condition for differentiability of the velocity field. In other situations of marginality (e.g., in critical phenomena), it is often found that there are logarithmic corrections to

power-law scaling, and this may be thought of as the origin of Kraichnan's logarithmic correction to the k^{-3} enstrophy cascade scaling of $E(k)$.

2.1 Wave-packet Model

The wave-packet model introduced by Ref. [21] has been used to study the wavenumber spectrum of finite-lifetime passive scalars in Lagrangian chaotic flows [22]. The passive nature of the high k components of the vorticity field allows use to be made of the results in Ref. [22] in studies of two-dimensional turbulence with drag [11, 10]. We will now give a brief review of the aspect of the wave-packet model that is important to our current work.

The advection of a passive scalar $\phi(\vec{x},t)$ by an incompressible flow $\vec{v}(\vec{x},t)$ is governed by

$$\frac{\partial\phi}{\partial t} + \vec{v}\cdot\nabla\phi = \kappa\nabla^2\phi - \mu\phi + f_\phi(\vec{x},t) \ , \tag{2.2}$$

where κ is the diffusivity of the scalar and f_ϕ represents a source of the scalar. Note that we use the same symbol μ both for the passive scalar decay rate (μ^{-1}= average lifetime) in Eq. (2.2) and for the frictional drag coefficient in Eq. (1.1). The system size is taken to be $L\times L$. We first consider the case when both diffusion and source are absent and $\phi(\vec{x},0)=\phi_0(\vec{x})$. This is equivalent to the situation when the source is turned on momentarily at $t=0$, or $f_\phi(\vec{x},t)=\phi_0(\vec{x})\delta(t)$ with $\phi(\vec{x},t)=0$ for $t<0$. In the wave-packet model, we imagine that the scalar field is composed of a number of localized sinusoidal wave-packets $\phi_j(\vec{x},t)$. Each wave-packet has a characteristic wavenumber $\vec{k}_j(t)$, is localized in a region $\mathcal{B}_j$ of length scale much smaller than $1/k_f$, and is centered at $\vec{x}_j(t)$. Specifically, we have $\phi=\sum_j\phi_j$ with

$$\phi_j(\vec{x},t) = A_j(t)\exp\{i[\vec{k}_j(t)\cdot\vec{x}+\theta_j(t)]\} \tag{2.3}$$

and $A_j(t)$ is negligibly small for $\vec{x}$ outside $\mathcal{B}_j$. The evolution of each wave-packet is governed by the following set of equations:

$$\frac{d\vec{x}_j(t)}{dt} = \vec{v}(\vec{x}_j(t),t) \ , \tag{2.4}$$

$$\frac{d\vec{k}_j(t)}{dt} = -(\nabla\vec{v})\cdot\vec{k}_j(t) \ , \tag{2.5}$$

$$\frac{d\Omega_j(t)}{dt} = -2\mu\Omega_j(t) \ , \tag{2.6}$$

where $\Omega_j(t) = 1/L^2 \int \phi_j^2 \, d\vec{x}$ is the variance of the wave packet. Eq. (2.4) gives the position of a wave-packet as it is advected along a fluid trajectory. Eq. (2.6) follows from Eq. (2.2) with κ and f_ϕ set to zero. To derive Eq. (2.5), consider two trajectories initially separated by the infinitesimal vector $\delta\vec{x}_j(0)$. The time evolution of the scalar difference $\delta\phi_j = \delta\vec{x}_j \cdot \nabla\phi_j = \delta\vec{x}_j \cdot (i\vec{k}_j\phi_j)$ along these trajectories is given by

$$\frac{d\,\delta\phi_j}{dt} = -\mu\,\delta\phi_j \tag{2.7}$$

which implies

$$\frac{d}{dt}[\vec{k}_j(t) \cdot \delta\vec{x}_j(t)] = 0\,. \tag{2.8}$$

From Eq. (2.4) and the assumption that the velocity field is smooth, we have

$$\frac{d\,\delta\vec{x}_j(t)}{dt} = (\delta\vec{x}_j(t) \cdot \nabla)\vec{v}\,. \tag{2.9}$$

Eq. (2.5) then follows from Eq. (2.8) and Eq. (2.9).

To get a better picture of the evolution of the wave-packets, we focus on one of the wave-packets and drop the subscript j. In general the differential equation for $\delta\vec{x}(t)$, Eq. (2.9) will have two linearly independent solutions, $\delta\vec{x}_1(t)$ and $\delta\vec{x}_2(t)$. Therefore, we can write $\delta\vec{x}(t) = \beta_1\delta\vec{x}_1(t) + \beta_2\delta\vec{x}_2(t)$ where β_1 and β_2 are constants. Since the fluid motion is incompressible, the area of the parallelogram defined by $\delta\vec{x}_1$ and $\delta\vec{x}_2$, $J = \hat{z} \cdot \delta\vec{x}_1 \times \delta\vec{x}_2$, is a constant. Thus, $\delta\vec{x}_1$ and $\delta\vec{x}_2$ can be chosen in such a way that $|\delta\vec{x}_1|$ is exponentially increasing, while $|\delta\vec{x}_2|$ is exponentially decreasing, and for large t we have

$$|\delta\vec{x}_1(t)| \sim |\delta\vec{x}_1(0)|e^{h(t;\vec{x}_0)t}\,. \tag{2.10}$$

Now let us express the wave vector $\vec{k}(t)$ in terms of the reciprocal basis,

$$\vec{k}(t) = \alpha_1(\delta\vec{x}_1 \times \hat{z}) + \alpha_2(\hat{z} \times \delta\vec{x}_2)\,. \tag{2.11}$$

Eq. (2.8) implies that $\vec{k}(t) \cdot \delta\vec{x}(t) = J(\alpha_1\beta_2 - \alpha_2\beta_1)$ is independent of time. It then follows that α_1 and α_2 are constants. Therefore $\vec{k}(t)$ may be written as

$$\begin{aligned}\vec{k}(t) = \frac{1}{J} \quad & \Big\{\delta\vec{x}_2(0) \cdot \vec{k}(0)[\hat{z} \times \delta\vec{x}_1(t)] \\ & - \delta\vec{x}_1(0) \cdot \vec{k}(0)[\hat{z} \times \delta\vec{x}_2(t)]\Big\}\ .\end{aligned} \tag{2.12}$$

This shows that $\vec{k}(t)$ also consists of an exponentially increasing and an exponentially decreasing component, the increasing component of $\vec{k}(t)$ being perpendicular to that of $\delta\vec{x}_1(t)$. For large enough t, we thus have the following approximation,

$$|\vec{k}(t)| \sim |\vec{k}(0)|e^{h(t;\vec{x}_0)t}\,. \tag{2.13}$$

From the above discussion, we see that, as a wave-packet moves along a fluid trajectory, it is stretched in one direction and compressed in another, while keeping its area constant; the component of the wave vector along the direction of contraction increases exponentially, indicating the development of fine structure in that direction.

2.2 Distribution of Finite-time Lyapunov Exponent

As mentioned earlier, the exponential divergence of nearby trajectories in a chaotic flow over a time interval 0 to t can be quantified by a finite-time Lyapunov exponent $h(t;\vec{x}_0)$ defined in Eq. (1.13). In the limit $t \to \infty$, $h(t;\vec{x}_0)$ will approach the usual infinite-time Lyapunov exponent $\bar{h}$ for almost all initial conditions $\vec{x}_0$ and almost all initial orientations of $\delta\vec{x}$. At finite time, the dependence of h on $\vec{x}_0$ results in a distribution in the values of h which can be characterized by the conditional probability density function $P(h\,|\,t)$. That is, if $\vec{x}_0$ is chosen randomly with uniform density in the region of the fluid flow, and if the initial orientation of $\delta\vec{x}$ is arbitrarily chosen, then we can define a probability distribution $P(h\,|\,t)$ such that $P(h\,|\,t)dh$ is the probability that $h(t;\vec{x}_0)$ lies between h and $h+dh$. As t increases, $P(h\,|\,t)$ will become more and more sharply peaked at $\bar{h}$ and approach a delta-function at $\bar{h}$ as $t \to \infty$. The distribution $P(h\,|\,t)$ plays an important role in our theory.

We can numerically approximate $P(h\,|\,t)$ as follows. After the flow has reached the steady-state, we initialize uniformly in space a large number of wave-packets into the flow at $t = t_0$. The wave-packets evolve according to Eq. (2.4) – Eq. (2.6) and $h(t;\vec{x}_j(t_0))$ is estimated using

$$h(t;\vec{x}_j(t_0)) = \frac{1}{t}\ln\frac{|\vec{k}_j(t+t_0)|}{|\vec{k}_j(t_0)|} \tag{2.14}$$

from Eq. (2.13). A histogram approximation to $P(h\,|\,t)$ can then be generated. In our computations, the initial wave vector $\vec{k}_j(t_0)$ was taken to be $\hat{x}+\hat{y}$ for all j. In order to obtain better statistics,

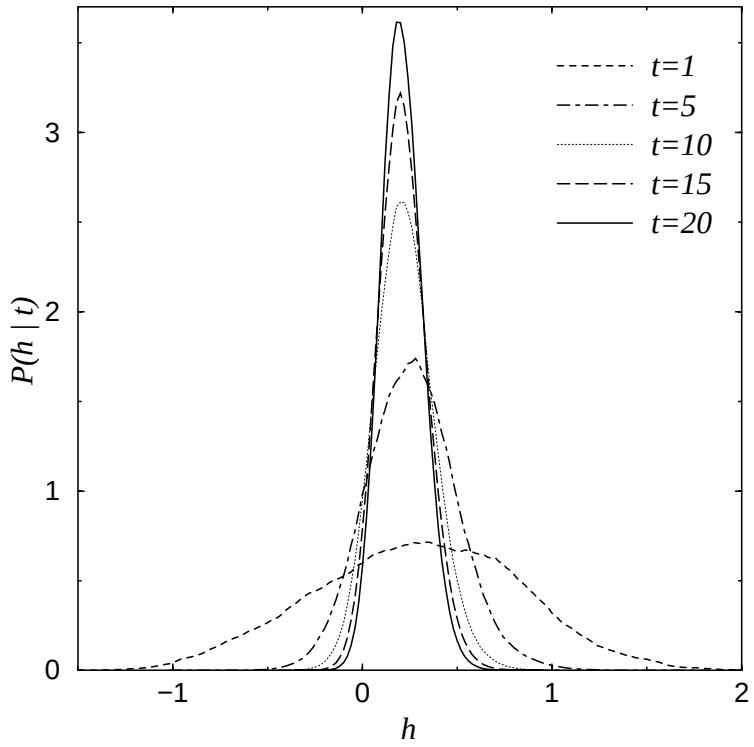

Figure 2.1: Probability distribution function of the finite-time Lyapunov exponent $P(h\,|\,t)$ for different time t for the case $\mu = 0.2$.

we inject one group of 1024^2 wave-packets into the flow every 1 time unit, so t_0 in Eq. (2.14) will be different for different groups. We launch a total of 16 groups and each group evolves for 20 time units. A histogram approximation to $P(h\,|\,t)$ is then calculated using the $h(t;\vec{x}_j(t_0))$ from all 16 groups. FIG. 2.1 shows $P(h\,|\,t)$ at different t for the case of $\mu = 0.2$. As time increases, $P(h\,|\,t)$ becomes sharply peak around a positive value of h showing that the flow is chaotic. In particular, for $t = 20$, $P(h\,|\,t)$ has its peak at $\bar{h} \approx 0.20$. The function $P(h\,|\,t)$ shows similar behavior for the case $\mu = 0.1$ with a peak occurring at $\bar{h} \approx 0.24$ for $t = 20$. The smaller damping in the latter case apparently allows the fluid to undergo bigger stretching in a given amount of time.

Based on the argument that $h(t;\vec{x}_0)$ can be considered as an average over many independent random realizations, $P(h\,|\,t)$ is approximated by the following asymptotic form [18],

$$P(h\,|\,t) \sim \sqrt{\frac{tG''(h)}{2\pi}}\, e^{-tG(h)} \tag{2.15}$$

for large t. Eq. (2.15) has been shown to be true for the generalized baker's map [23] and nu-

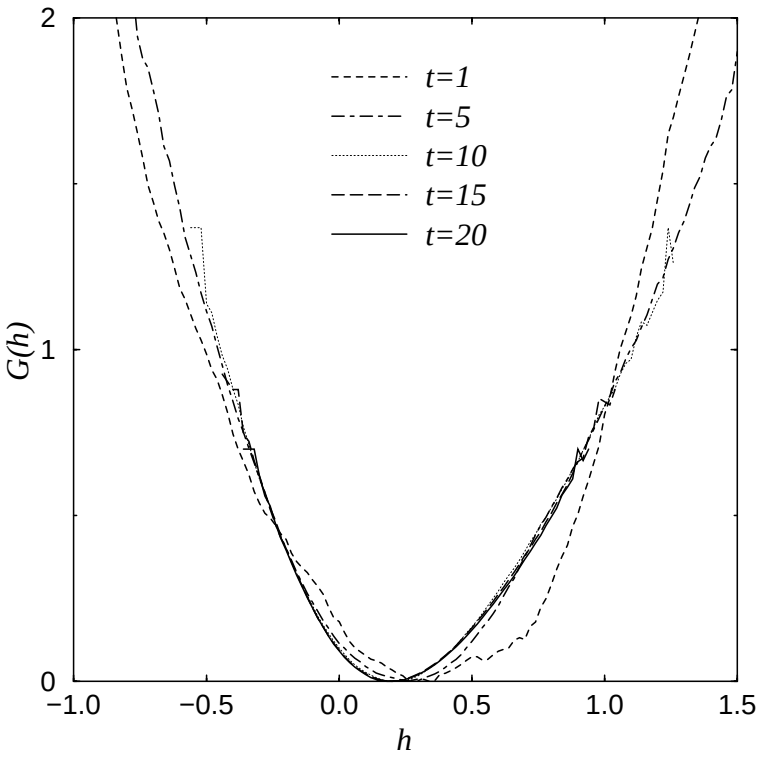

Figure 2.2: $G(h)$ (see Eq. (2.15)) for different time t for the case $\mu = 0.2$.

merically verified for cases where there are no KAM surfaces, for example, see Ref. [24]. The function $G(h)$ is concave upward, $G''(h) \geq 0$. It has the minimum value zero, occurring at $h = \bar{h}$, $G'(\bar{h}) = G(\bar{h}) = 0$. The significance of Eq. (2.15) is that it expresses a function of two variables $P(h\,|\,t)$ in terms of a function of a single variable $G(h)$. Eq. (2.15) will be used in the development of the theory.

The function $G(h)$ can be approximated at large t from $P(h\,|\,t)$ using the following relation,

$$G(h) \approx K - \frac{1}{t} \ln P(h\,|\,t) \ , \tag{2.16}$$

where K is determined by the condition that the minimum of $G(h)$ equals zero. FIG. 2.2 shows the $G(h)$ obtained from the corresponding $P(h\,|\,t)$ shown in FIG. 2.1. The large number ($1024^2 \times 16 = 4096^2$) of wave-packets used in the generation of each $P(h\,|\,t)$ allows us to obtain $G(h)$ for a large range of h. As can be seen in FIG. 2.2, for large enough t, the graphs of $G(h)$ for different t more or less collapse onto each other, showing that Eq. (2.15) is a good approximation to $P(h\,|\,t)$ for the flows we considered. $G(h)$ shows similar behavior in the case $\mu = 0.1$.

Chapter 3 Energy Wavenumber Spectrum

3.1 Review of Theory

In Ref. [22], an expression relating $G(h)$ and the scaling exponent of the power spectrum of a finite-lifetime passive scalar [25, 19] in a Lagrangian chaotic flow is derived. Using the results in Ref. [22] and the assumption that the large k components of the vorticity field act like a passive scalar, a similar expression for ξ can be derived [11, 10]. In this section, we review this theory.

The power spectrum of a passive scalar $E_\phi(k,t)$ is defined as

$$E_\phi(k,t) = \int \frac{d\vec{k}'}{(2\pi)^2}\,\delta(|\vec{k}'|-k)\frac{|\tilde{\phi}(\vec{k},t)|^2}{L^2}\,, \tag{3.1}$$

where L is the periodicity length, and $\tilde{\phi}(\vec{k},t)$ is the Fourier transform of $\phi(\vec{x},t)$,

$$\tilde{\phi}(\vec{k},t) = \int d\vec{x}\,\phi(\vec{x},t)\,e^{-i\vec{k}\cdot\vec{x}}\,. \tag{3.2}$$

In the wave-packet model, $|\tilde{\phi}_j|^2 = |A_j|^2\delta_l(\vec{k}-\vec{k}_j)$ where δ_l is a function of width l^{-1} centered at $k = |\vec{k}_j(t)|$. With $f_\phi = 0$, we have $|\tilde{\phi}|^2 = |\sum_j \tilde{\phi}_j|^2 \approx \sum_j |\tilde{\phi}_j|^2$. We have assumed l^{-1} is small enough that we can neglect the overlap between different $\tilde{\phi}_j(\vec{k},t)$. Noting that $\Omega_j(t) \sim |A_j(t)|^2$, $E_\phi(k,t)$ for $f_\phi = 0$ can be then written as

$$E_\phi(k,t) \sim \sum_j \Omega_j(t)\,\delta(|\vec{k}_j(t)|-k)\,. \tag{3.3}$$

The presence of a statistical steady external source at the large scale corresponds to the situation in which wave-packets are continuously launched at small k. Each small area then consists of many overlapping wave-packets created at a different time $\tilde{t}$, thus

$$\phi(\vec{x},t) = \sum_j \frac{1}{T}\int_0^t d\tilde{t}\;\phi_j(\vec{x},t;\tilde{t})\;, \tag{3.4}$$

where $\phi_j(\vec{x},t;\tilde{t})$ denotes a wave-packet at time t that is launched at time $\tilde{t}$, the summation is over all the wave-packets launched at $\tilde{t}$, T is a constant depending on the properties of the source and has the dimension of time. Assuming the wave-packets evolve independently, we can approximate the sum over wave-packets launched at different times by summing over the various stages of

evolution of the wave-packets launched at time zero,

$$\sum_j \int_0^t d\tilde{t}\ \phi_j(\vec{x},t;\tilde{t}) \approx \sum_j \int_0^t dt'\ \phi_j(\vec{x},t')\,. \tag{3.5}$$

We have used the notation $\phi_j(\vec{x},t') = \phi_j(\vec{x},t';0)$ in Eq. (3.5). Therefore, in the presence of a source, the power spectrum of the scalar is given by

$$E_\phi(k,t) \sim \int_0^t dt' \sum_j \Omega_j(t')\,\delta(|\vec{k}_j(t')| - k)\,. \tag{3.6}$$

We consider the time asymptotic spectrum $E_\phi(k) = E_\phi(k, t\to\infty)$. Assuming $\Omega_j(0) = \Omega_0$ and $|\vec{k}_j(0)| = k_0$ for all j and using Eq. (2.13), we have

$$\begin{aligned} E_\phi(k) &\sim \int_0^\infty dt' \sum_j \Omega_0\, e^{-2\mu t'}\,\delta(k - k_0 e^{h_j t'}) \\ &\sim \int_0^\infty dt' \int dh\, P(h\,|\,t') e^{-2\mu t'}\,\frac{\delta(t'-\lambda/h)}{hk}\ , \end{aligned} \tag{3.7}$$

where $\lambda = \ln(k/k_0)$, and we have replaced the summation over wave-packets with an integration over the probability density function for finite-time Lyapunov exponents. We use the asymptotic form Eq. (2.15) for $P(h\,|\,t)$ and perform the integrations. For large k, we have $\lambda \gg 1$ and the integral over h can be evaluated using the steepest descent method. We thus obtain

$$E_\phi(k) \sim k^{-(1+\xi)}\,, \tag{3.8}$$

with ξ given by

$$\xi = \min_h \left\{ \frac{G(h) + 2\mu}{h} \right\}. \tag{3.9}$$

We now consider the energy density $e(\vec{k})$ which is given by

$$e(\vec{k}) = \frac{1}{(2\pi)^2}\,\frac{|\tilde{v}_x(\vec{k})|^2 + |\tilde{v}_y(\vec{k})|^2}{2L^2}\,, \tag{3.10}$$

where $\tilde{v}_x(\vec{k})$ and $\tilde{v}_y(\vec{k})$ are Fourier transforms of the x and y components of the velocity field $\vec{v}(x,y)$. The wavenumber energy spectrum $E(k)$ is then defined as

$$E(k) = \int d\vec{k}'\delta(|\vec{k}'| - k) e(\vec{k}')\,. \tag{3.11}$$

From $\omega = \hat{z}\cdot\nabla\times\vec{v}$, we have $\tilde{\omega}(\vec{k}) = ik_x\tilde{v}_y(\vec{k}) - ik_y\tilde{v}_x(\vec{k})$. Thus, using the isotropic assumption, $E(k)$ is related to the power spectrum of the vorticity $E_\omega(k)$ by $E(k) = 2k^{-2}E_\omega(k)$. Hence, applying

the passive scalar results to the vorticity, we obtain

$$E(k) \sim k^{-(3+\xi)}\,, \tag{3.12}$$

with ξ given by Eq. (3.9). We note that, as can be seen from Eq. (2.5) and Eq. (2.14), $G(h)$ is completely specified by the flow $\vec{v}(\vec{x},t)$. Hence, $G(h)$ will depend on the value of μ in the case of vorticity but is independent of μ in the passive scalar case.

3.2 Comparison of Theory and Numerical Results

To apply our theory to determine the energy spectrum scaling exponent of our turbulent flow governed by Eq. (1.2), $G(h)$ for sufficiently large t is obtained numerically as described in Chapter 2. ξ is then determined from Eq. (3.9), denoted as ξ_{th}, using a fourth degree polynomial fit of the numerically obtained $G(h)$. The quadratic approximation to $G(h)$, which corresponds to a Gaussian distribution of h, is not adequate for the determination of ξ_{th} and the vorticity structure function scaling exponents ζ_{2q} to be discussed in the subsequent chapters. This is because the main contribution to the integrals involved comes from saddle points $h = h^*$ which can be many standard deviations away from $\bar{h}$. FIG. 3.1 shows $G(h)$ at large t for $\mu(k > 6) = 0.1$ and for $\mu(k > 6) = 0.2$ together with the polynomial fits. The resulting values of ξ_{th} obtained are shown in TABLE 3.1. The difference between the two $G(h)$ shown in FIG. 3.1 is relatively small. This is because, as mentioned in Chapter 2, h is mainly determined by the small k components of the flow, and we have used the same value $\mu = 0.1$ for $k \leq 6$ in our simulations.

To verify the theoretical results, we compute the energy spectrum directly from the numerical solution of Eq. (1.2) on a 4096×4096 grid using Eq. (3.11), which can be written in terms of

Table 3.1: Comparison of the values of ξ obtained from numerical simulations to the theoretical results.

$\mu(k > 6)$	$\xi_{th}(= \zeta_{2,th})$	ξ_{DNS}	$\zeta_{2,DNS}$	$\zeta_{2,E(k)}$
0.1	0.57	0.61	0.66	0.68
0.2	1.12	1.12	1.16	1.14

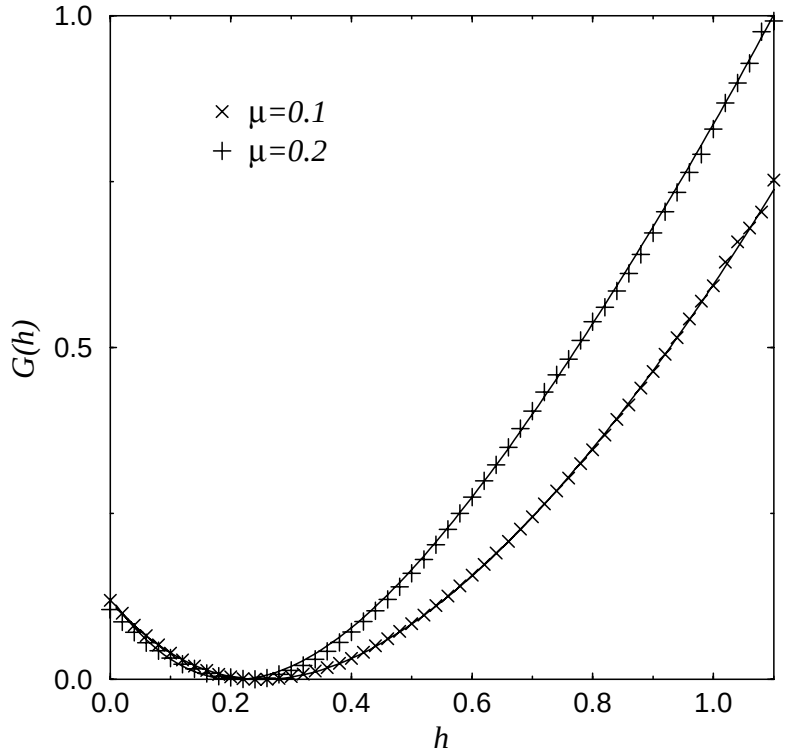

Figure 3.1: $G(h)$ for $\mu = 0.1$ (at t=12) and $\mu = 0.2$ (at t=8). The solid lines are fourth degree polynomial fits: for μ=0.1, $G(h) \approx 0.12 - 1.01h + 2.46h^2 - 1.35h^3 + 0.38h^4$; for $\mu = 0.2$, $G(h) \approx 0.13 - 1.30h + 3.90h^2 - 2.64h^3 + 0.75h^4$.

the vorticity as

$$E(k,t) = \int \frac{d\vec{k}'}{(2\pi L)^2}\,\delta(|\vec{k}'| - k)\frac{|\tilde{\omega}(\vec{k}',t)|^2}{2|\vec{k}'|^2} \tag{3.13}$$

where $\tilde{\omega}(\vec{k}',t)$ is the Fourier transform of $\omega(\vec{x},t)$. The time averaged energy spectrum $E(k)$ is obtained by averaging $E(k,t)$ at every 0.1 time unit from $t = 41$ to $t = 75$. FIG. 3.2 shows a log-log plot of $E(k)$ versus k for the two different values of μ we considered. In both cases, a clear scaling range of more than a decade can be observed. We measure the scaling exponents by linearly fitting $E(k)$ in the scaling range. The results, denoted ξ_{DNS}, are shown in TABLE 3.1. Good agreement is found between the numerical and the theoretical results. These results are consistent with those of previous work in [11] and [13] which use grids of 1024×1024 and 2048×2048, respectively.

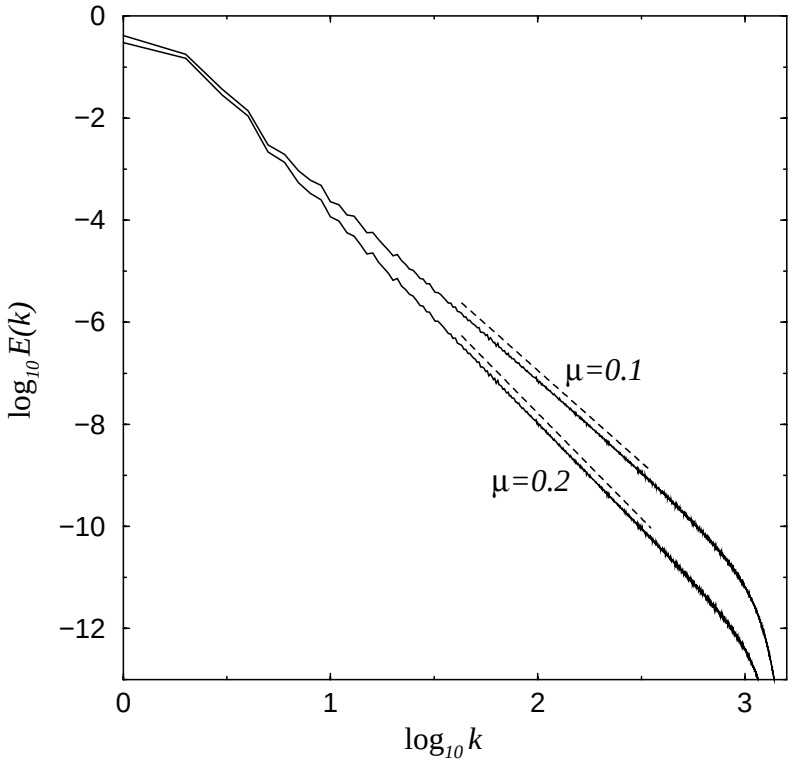

Figure 3.2: Energy wavenumber spectra. The dotted lines are the corresponding linear fit in the scaling range.

3.3 Discussion

The presence of drag gives a power law for the energy spectrum that falls faster than the case without drag and ξ is the correction to the classical zero drag value of the scaling exponent. Note that the major contribution to the integral Eq. (3.7) comes from the immediate neighborhood of $h = h_1^*$, where h_1^* is the value of h at which the minimum of $G(h)/h + 2\mu/h$ occurs. As $\mu \to 0$, $h_1^* \to \bar{h}$ and hence $\xi \to 0$. The scaling exponent is thus determined by the majority of wave-packets with stretching rate close to $\bar{h}$. On the other hand, for $\mu \neq 0$, $h_1^* > \bar{h}$ (cf. Section 4.1). Therefore the scaling exponent is determined by a small number of wave-packets that experience a stretching rate h_1^*, that is larger than the typical stretching rate $\bar{h}$, and h_1^* increases with μ (h_1^* for $\mu = 0.1$ and $\mu = 0.2$ are 0.47 and 0.57 respectively). The reason for this is that due to drag, the variance of the wave-packets decrease exponentially with time. Thus, as can be seen from the first line of Eq. (3.7), the main contribution to $E(k)$ is from the variance of those wave-packets with smaller

$\mu t'$. Thus the wave-packets that contribute most to $E(k)$ at a certain fixed k(or λ) are those with larger stretching rate. It should also be clear from the above discussion that, in order to get an accurate estimate to ξ, it is important to take into account the fluctuation in the finite-time Lyapunov exponent. If we were to neglect the fluctuation and take the stretching rate to be $\bar{h}$ for all wave-packets, we would have overestimate ξ to be $2\mu/\bar{h}$ (which equals 0.83 and 2.0 for $\mu = 0.1$ and $\mu = 0.2$, respectively).

Chapter 4 Vorticity Structure Functions

4.1 Review of Theory

We now consider the scaling of the vorticity structure functions in the limit $\nu \to 0^+$. The results have previously been given in Ref [19], which treats finite-lifetime passive scalars rather than vorticity in two-dimensional turbulence with drag, and in Ref [13] for two-dimensional turbulence with drag. Here, for completeness, we derive the previous results (our derivation is different from that in Ref [19] and more complete than that in Ref [13]).

The initial condition for the vorticity field is taken to be $\omega(\vec{x}, 0) = 0$. Recall from Section 2.1 that, at each point of the flow, there is an expansion direction $\delta\vec{x}_1$ and a contraction direction $\delta\vec{x}_2$. Going backward in time, the distance between two nearby trajectories separated by $\vec{r}$ at time t will expand along $\delta\vec{x}_2$ and contract along $\delta\vec{x}_1$. The vorticity difference, $\delta_{\vec{r}}\omega(\vec{x}, t)$ between the two points $\vec{x}$ and $\vec{x} + \vec{r}$ depends on the history of the trajectories leading to these points. From Eq. (1.2),

$$\delta_{\vec{r}}\omega(\vec{x}, t) = e^{-\mu t} \int_0^t \delta f_\omega[\vec{x}(t')] e^{\mu t'} dt' \ , \tag{4.1}$$

where $\delta f_\omega[\vec{x}(t')] = f_\omega[\vec{x}(t') + \delta\vec{x}(t')] - f_\omega[\vec{x}(t')]$, $\vec{x}(t')$ and $\vec{x}(t') + \delta\vec{x}(t')$ are the two trajectories that pass through $\vec{x}$ and $\vec{x} + \vec{r}$ at $t' = t$, $\vec{x}(t) = \vec{x}, \vec{x}(t) + \delta\vec{x}(t) = \vec{x} + \vec{r}$. We break the integral Eq. (4.1) into two parts by defining a time $\tau(r)$ such that, going backwards in time from t to $t - \tau(r)$, the separation $\vec{r}$ grows to be of the order of the spatial scale L over which $f_\omega(\vec{x})$ varies, $re^{h\tau} \sim L$, where h here denotes the time τ finite-time Lyapunov exponent associated with the point $\vec{x}$ and the time interval $(t - \tau, t)$. Hence,

$$\begin{aligned} \delta_{\vec{r}}\omega(\vec{x}, t) \quad \sim \quad & \vec{r} \cdot \int_{t-\tau(r)}^{t} \nabla f_\omega[\vec{x}(t')] e^{(\mu - h)(t' - t)} dt' \\ & + \int_0^{t-\tau(r)} \delta f_\omega[\vec{x}(t')] e^{\mu(t' - t)} dt' \ . \end{aligned} \tag{4.2}$$

We have linearized $\delta f_\omega[\vec{x}(t')]$ for $t - \tau(r) < t' < t$ when the two trajectories are close together, and used the relation $\delta\vec{x}(t') \sim \vec{r}e^{h(t-t')}$, this gives the first term in Eq. (4.2). The remaining integral can be estimated as follows. Since $f_\omega(\vec{x})$ varies on the large scale L, the quantity $\delta f_\omega[\vec{x}(t')]$ has a

maximum magnitude equal to that corresponding to the range of variation of $f_\omega(\vec{x})$ as a function of $\vec{x}$, we denote this value f_0. Also, $\delta f_\omega[\vec{x}(t')]$ oscillates on the largest spatial scale turnover time for $t' < t - \tau(r)$. Thus the second integral in Eq. (4.2) is of order $\mu^{-1} f_0 e^{-\mu\tau} \sim (r/L)^{\mu/h}$. Estimating ∇f_ω to be of the order of f_0/L, we see that if $h > \mu$, the first integral is of the order of $\mu^{-1}(r/L) f_0 e^{-(\mu-h)\tau} \sim (r/L)^{\mu/h} \sim e^{-\mu\tau}$ which is the same order of magnitude estimate as we obtained for the second integral. On the other hand, if $h < \mu$, our estimate of the first integral is $\mu^{-1}(r/L) f_0 \sim r/L \sim e^{-h\tau}$. Thus

$$|\delta_{\vec{r}}\omega|^{2q} \sim \begin{cases} O\left(e^{-2q\mu\tau}\right) & \text{if} \quad h > \mu \\ \\ O\left(e^{-2qh\tau}\right) & \text{if} \quad h < \mu \ . \end{cases} \tag{4.3}$$

We take the average of Eq. (4.3) over $\vec{x}$ and then replace this average by an average over τ at fixed exponentiation $\lambda = \ln(L/r) = h\tau$. Introducing the conditional probability density $R(\tau \,|\, \lambda)$ of τ for a fixed λ, We find

$$S_{2q}(r) \sim \int_0^{\frac{\lambda}{\mu}} d\tau \, R(\tau \,|\, \lambda) e^{-2q\mu\tau} + \int_{\frac{\lambda}{\mu}}^{\infty} d\tau \, R(\tau \,|\, \lambda) e^{-2q\lambda} \ . \tag{4.4}$$

Using the following relation between $R(\tau \,|\, \lambda)$ and $P(h \,|\, \tau)$ [26],

$$R(\tau \,|\, \lambda) \approx \frac{d}{d\tau} \int_{\frac{\lambda}{\tau}}^{\infty} dh \, P(h \,|\, \tau) \tag{4.5}$$

and the asymptotic form Eq. (2.15) for $P(h \,|\, \tau)$, the integral Eq. (4.4) is performed using the steepest descent method with λ as the large parameter. The result is that the structure function scaling exponents, ζ_{2q} defined in Eq. (1.4), is given by

$$\zeta_{2q} = \min_h \{2q, H_q(h)\} \ , \tag{4.6}$$

where

$$H_q(h) = \frac{G(h) + 2q\mu}{h} \ . \tag{4.7}$$

This result has been previously obtained in Refs. [19] and [13]. Thus, we have related ζ_{2q} to the properties of the flow, namely the drag coefficient μ and the distribution of the finite-time Lyapunov exponent h.

Let $h = h_q^*$ be the value of h at which $H_q(h)$ is minimum. We now show that h_q^* increases with q. Letting $\beta > \alpha$, by the definition of h_q^*, $H'_\alpha(h_\alpha^*) = H'_\beta(h_\beta^*) = 0$, it follows that $G'(h_\beta^*) - H_\beta(h_\beta^*) =$

$G'(h^*_\alpha) - H_\alpha(h^*_\alpha)$. Since $H_\beta(h) > H_\alpha(h)$ for all h, we have $G'(h^*_\beta) > G'(h^*_\alpha)$ which implies $h^*_\beta > h^*_\alpha$ due to the fact that $G''(h) > 0$ for all h. Moreover, putting $\alpha = 0$ gives $h^*_q > \bar{h}$ for all q as mentioned in Section 3.3.

4.2 Comparison of Theory and Numerical Results

Numerical tests of theoretical predictions of structure function exponents of finite-lifetime passive scalar fields advected by simple chaotic flows have been performed in Ref [19] and [13]. To test the analogous theoretical predictions, Eq. (4.6) and Eq. (4.7), in the case of two-dimensional turbulence with drag, we define the averaged structure functions of order $2q$ as

$$S_{2q}(r) = \int \frac{d\vec{r}\,'}{2\pi r} \delta(r - |\vec{r}\,'|) \langle\, |\delta_{\vec{r}'}\omega|^{2q} \rangle \ . \tag{4.8}$$

The angled brackets denote average over the entire region occupied by the fluid. The angular dependence of $\langle\, |\delta_{\vec{r}'}\omega|^{2q} \rangle$ is averaged out in Eq. (4.8) by the integration over $\vec{r}\,'$. Using Eq. (4.8) with $\omega(\vec{x}, t)$ obtained from the numerical integration of Eq. (1.2), we compute $S_{2q}(r)$ from $t = 41$ to $t = 75$ at every 1 time unit and take the average of the results obtained.

Following the scheme described above, we calculate the time-averaged structure functions for q ranging from 0.0 to 2.0. FIGS. 4.1(a) and 4.2(a) show samples of the results for the cases μ =0.1 and 0.2, respectively. The distance r is measured in the unit of grid size. For all values of q we have studied, the structure functions show a clear scaling range that is long enough to allow an estimate of the scaling exponents, ζ_{2q}. The scaling range of the structure functions in the real space roughly corresponds to that of the energy spectrum in the k-space. The values of ζ_{2q} are obtained by measuring the slope of the structure functions in the scaling range using a linear fit. Results for ζ_{2q}/ζ_2 are shown as circles in FIGS. 4.1(b) and 4.2(b). The measured values of ζ_2, denoted as $\zeta_{2,DNS}$, are given in TABLE 3.1. We then compute ζ_{2q} theoretically from Eq. (4.6), following the procedure we use to calculate ξ_{th} as described in Section 3.2. We again use the fourth degree polynomial fits of $G(h)$ shown in FIG. 3.1 in our calculations. The results are shown as crosses in FIG. 4.1(b) and 4.2(b) for the two cases of μ we studied. The predicted values of ζ_2, denoted as $\zeta_{2,th}$, are given in TABLE 3.1. The numerical and theoretical results agree reasonably well for

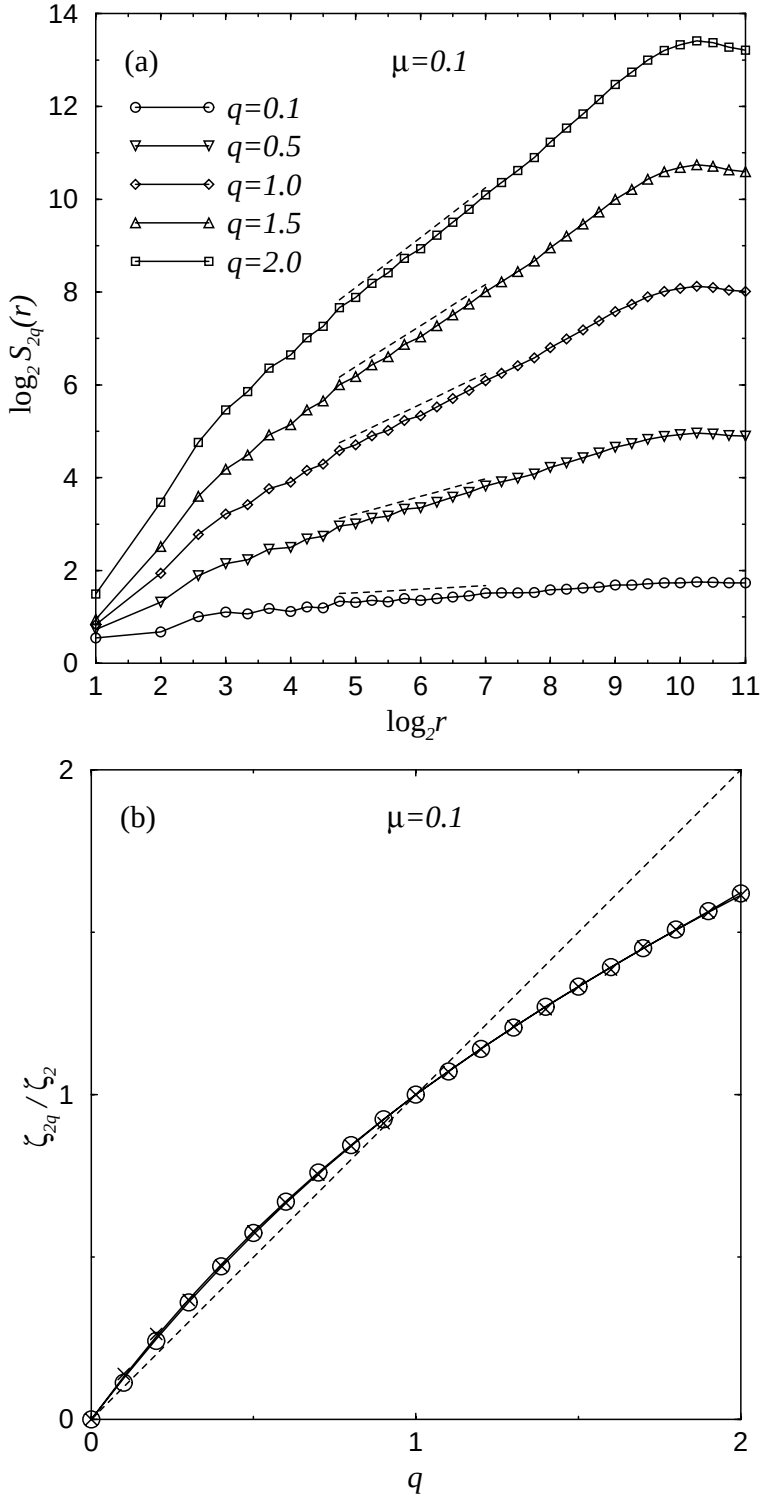

Figure 4.1: For the case of $\mu = 0.1$: (a) structure functions of vorticity difference, for various orders q between 0.1 and 2.0; the dotted lines are linear fits in the scaling range. (b) Plot of ζ_{2q}/ζ_2 obtained from numerical simulations (circle) and from Eq. (4.6) (cross), for different values of q; the solid lines are fourth degree polynomial fits to the circles and the crosses (cf. Eq. (6.14).)

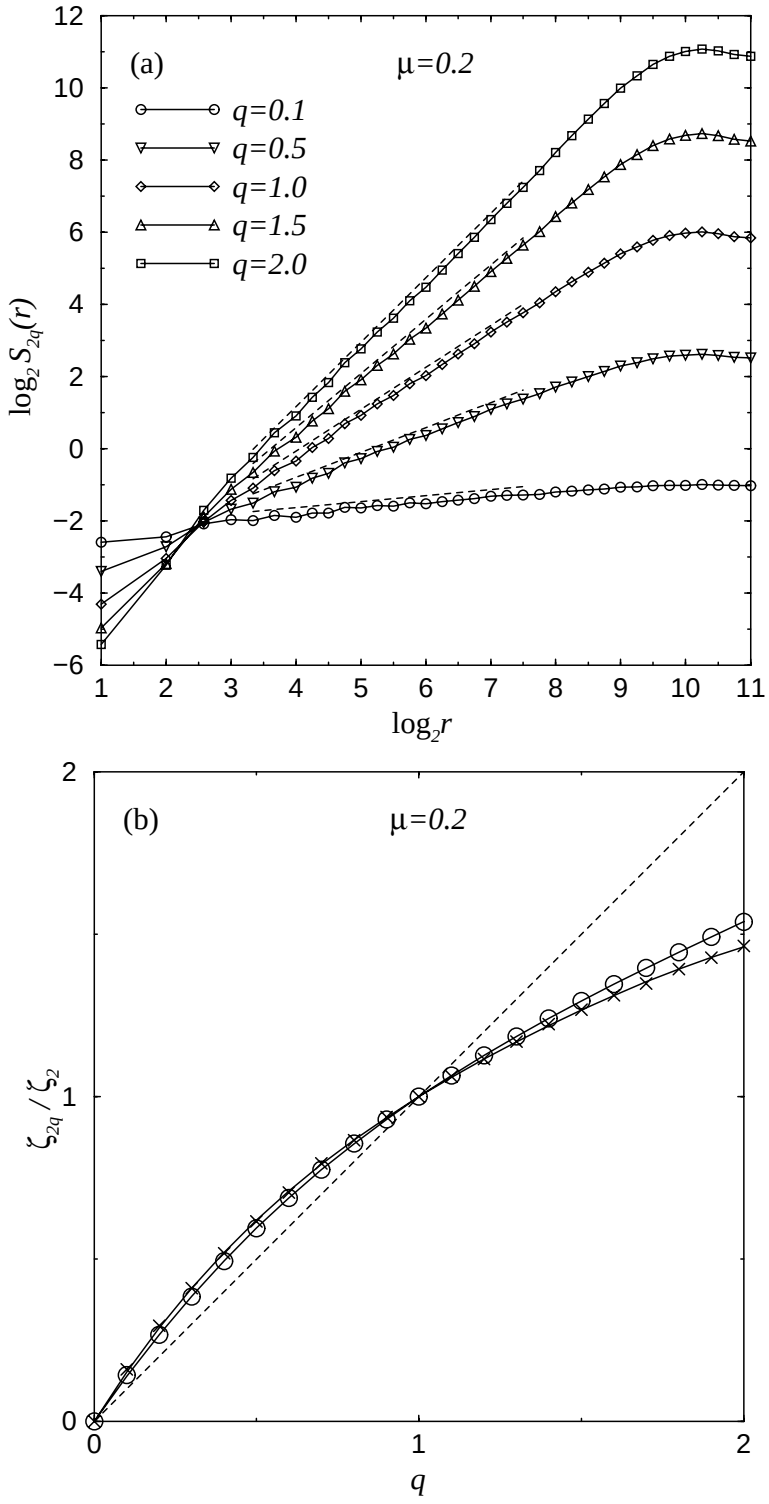

Figure 4.2: For the case of $\mu = 0.2$: (a) structure functions of vorticity difference, for various orders q between 0.1 and 2.0; the dotted lines are linear fits in the scaling range. (b) Plot of ζ_{2q}/ζ_2 obtained from numerical simulations (circle) and from Eq. (4.6) (cross), for different values of q; the solid lines are fourth degree polynomial fits to the circles and the crosses (cf. Eq. (6.14).)

all q's. In reference to Eq. (4.6) we note that, for all the cases we numerically tested, we found that $\zeta_{2q} = \min\{H_q(h)\} < 2q$ for all q. This is consistent with the general result that for $\mu < \bar{h}$, $\min\{H_q(h)\} < H_q(\bar{h}) < 2q$. We note, however, that this need not hold in general, particularly for large μ.

4.3 Discussion

The theory predicts that when drag is present, an inertial range exists in which the vorticity structure functions $S_{2q}(r)$ exhibit power-law scaling. The scaling exponent ζ_{2q} is given by Eq. (4.6). In the absence of intermittency ζ_{2q} scales linearly with q and $\zeta_{2q}/\zeta_2 = q$, which is plotted as the straight dashed line in FIGS. 4.1(b) and 4.2(b). For $\mu > 0$, Eq. (4.6) predicts that ζ_{2q} varies nonlinearly with q, as shown in FIGS. 4.1(b) and 4.2(b). This anomalous scaling of $S_{2q}(r)$, which indicates the presence of intermittency in the system, is verified numerically in both cases.

The anomalous scaling of $S_{2q}(r)$ is the result of the combined effect of drag and non-uniform stretching of fluid elements. If all fluid elements have the same stretching rate, say $\bar{h}$, then $e^{-\mu\tau}$ becomes a constant and thus ζ_{2q} is proportional to $2q$. On the other hand, if $\mu = 0$, regardless of whether the stretching is uniform or not, $\zeta_{2q} = 0$. FIGS. 4.1(b) and 4.2(b) also suggest that $S_{2q}(r)$ shows larger deviation from the simple scaling behavior, $\zeta_{2q}/\zeta_2 = q$, as μ increases.

We remark that the statistical error in the predictions of the values of the higher order structure function scaling exponents is in general larger. This is because, as already mentioned, h_q^* increases with q, hence for large q, ζ_{2q} depends mostly on a rare number of wave packets with large h. Also, we find that the minimum of the function $H_q(h)$ becomes less prominent as q increases.

We now focus on the second order structure function $S_2(r)$. The following relation can be obtained from the definition of $S_2(r)$ and Eq. (3.1),

$$S_2(r) = 2\int dk\,[1 - J_0(kr)]E_\omega(k) \tag{4.9}$$

where J_0 is the zeroth order Bessel function of the first kind. Applying the isotropic assumption,

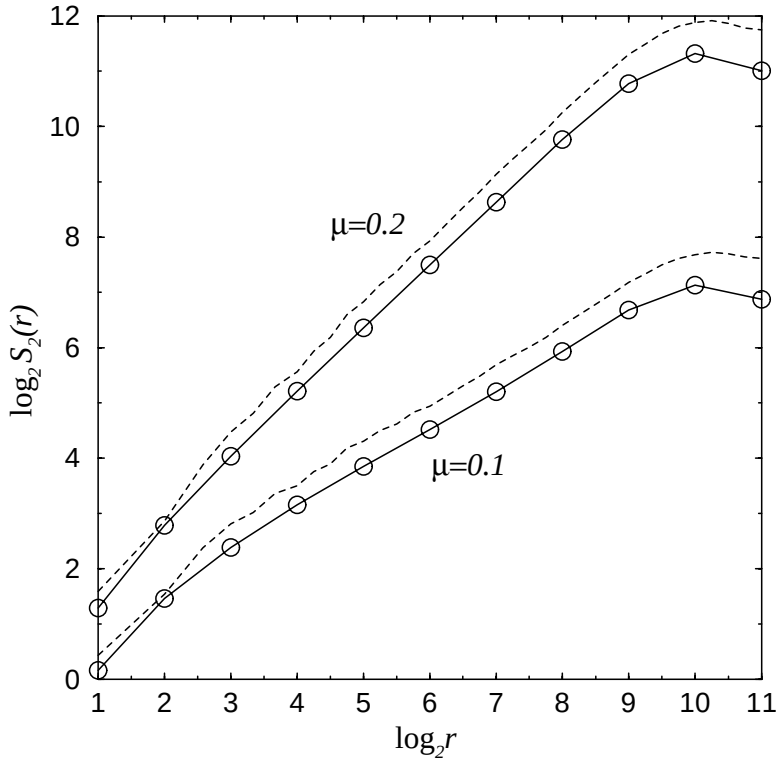

Figure 4.3: Second order structure functions $S_2(r)$ obtained from the energy spectrum $E(k)$ using Eq. (4.10) (solid line with circles) and from direct numerical simulations (dotted line).

$S_2(r)$ can then be related to the energy spectrum $E(k)$ by

$$S_2(r) = 4 \int dk \, [1 - J_0(kr)] k^2 E(k) \ . \tag{4.10}$$

We compute $S_2(r)$ by Eq. (4.10) using the $E(k)$ shown in FIG. 3.2. The results are plotted as solid lines in FIG. 4.3, the scaling exponents, denoted as $\zeta_{2,E(k)}$, are then measured and compared with $\zeta_{2,DNS}$ in TABLE 3.1. The $S_2(r)$ obtained directly from Eq. (4.8) are plotted as dashed lines in the same diagram for comparison. Ignoring viscosity at the small scales and forcing at the large scales, we can assume $E(k) \sim k^{-(3+\xi)}$ for all k. Then it follows from Eq. (4.10) that, for $0 < \xi < 2$, $S_2(r) \sim r^{\zeta_2}$ for all r and $\zeta_2 = \xi$. This is consistent with our theory which predicts that $\zeta_{2,th} = \xi_{th}$ when $0 < \zeta_{2,th} < 2$. Comparing $\zeta_{2,DNS}$ to ξ_{DNS}, we find reasonably good agreements but we note that $\zeta_{2,DNS}$ is in general slightly larger than ξ_{DNS}. We shall see that this small discrepancy is a result of the dependence of $S_2(r)$ on the large scales of the flow.

Due to the effects of forcing and viscosity, $E(k)$ deviates from the power-law behavior at

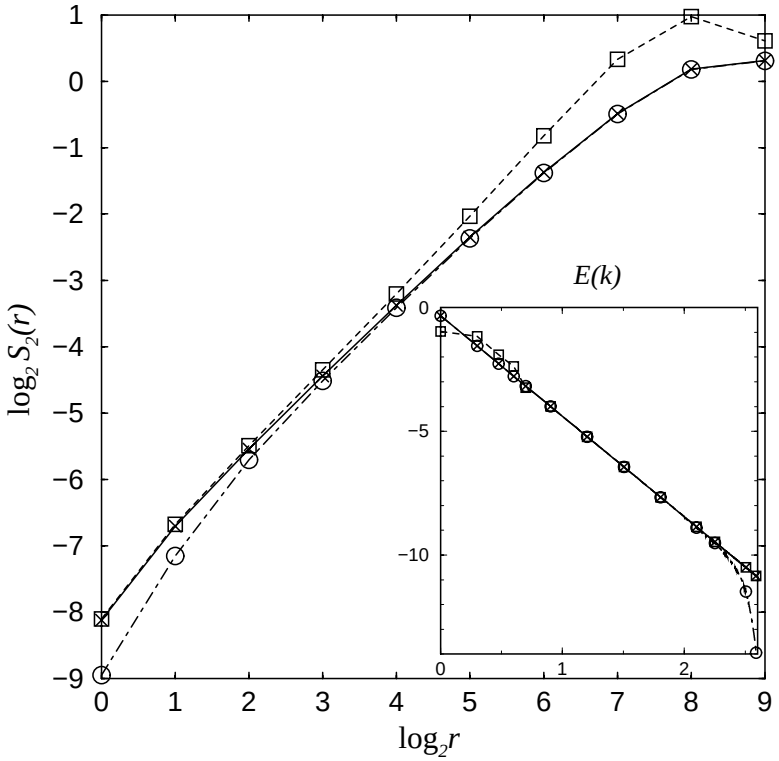

Figure 4.4: Second order structure functions $S_2(r)$ calculated by Eq. (4.10) using different $E(k)$: pure power law (cross), power law with small scales viscous cutoff (circle) and power law with large scales fluctuations (square). The inset shows the different $E(k)$ versus k with corresponding labels.

very small and very large k. According to Eq. (4.10), these deviations will affect $S_2(r)$. This is demonstrated in FIG. 4.4 in which we plot the $S_2(r)$ calculated by Eq. (4.10) using three different $E(k)$. The first one is a pure power law for all k. The second one is the same as the first one except it drops faster at large k mimicking the viscous cutoff. The third one is constructed from the first one by modifying the first five modes to mimic the presence of large scale forcing. The range of k used corresponds to a 1024×1024 lattice. From FIG. 4.4, it is seen that while the viscous effect is negligible except at small r, the large scale forcing can have a significant effect on the general shape of $S_2(r)$. As a result, $S_2(r)$ may have a very limited scaling range even when $E(k)$ shows a reasonably long one. We believe this is generally true for structure functions of any order, making it more difficult to accurately measure ζ_{2q} than ξ. We are able to obtain reliable estimates of ζ_{2q},

as verified by the agreement between $\zeta_{2,DNS}$ and ξ_{DNS}, by employing a 4096×4096 lattice and the time-averaging process.

Chapter 5 Probability Distribution of Vorticity Difference

5.1 Theory

In this section, we shall derive an expression for the probability distribution function $P_r(\delta_{\vec{r}}\omega)$ of the vorticity difference $\delta_{\vec{r}}\omega$ in terms of the conditional probability density function $R(\tau\,|\,\lambda)$. In Section 4.1, we introduced $R(\tau\,|\,\lambda)$ and deduce the scaling of $\delta_{\vec{r}}\omega$ by doing order of magnitude estimations of the integrals in Eq. (4.2). We now determine the distribution of $\delta_{\vec{r}}\omega$ by estimating the values of these integrals for different fluid trajectories. We shall assume the system is isotropic so that $P_r(\delta_{\vec{r}}\omega)$ depends on the distance r only, and not on the direction of $\vec{r}$.

Referring to Eq. (4.2), for $t-\tau < t' < t$, we estimate that $\vec{r}\cdot\nabla f_\omega[\vec{x}(t')] \sim (r/L) f_\omega[\vec{x}(t')] = e^{-\lambda} f_\omega[\vec{x}(t')]$. For $0 < t' < t-\tau$, the separation between the two trajectories is of order L and the values of $f_\omega[\vec{x}(t')]$ along the two trajectories become uncorrelated, hence $\delta f_\omega[\vec{x}(t')] \sim f_\omega[\vec{x}(t')]$. Approximating $f_\omega[\vec{x}(t')]$ as varying randomly, the values of the first and the second integral in Eq. (4.2) are respectively estimated as $[f_\omega/(\mu-h)](e^{-\lambda}-e^{-\mu\tau})$ and $(f_\omega/\mu)e^{-\mu\tau}$. This suggests that we can treat $\delta_{\vec{r}}\omega$ as a function of two random variables τ and $Z = f_\omega/\mu$ as follow,

$$\delta_{\vec{r}}\omega(Z,\tau) = Z\,\frac{e^{-\lambda}+e^{-\mu\tau}}{2}\ . \tag{5.1}$$

We then write the probability distribution function of $\delta_{\vec{r}}\omega$ as,

$$P_r(\delta_{\vec{r}}\omega) = \int_0^\infty P_r(\delta_{\vec{r}}\omega|\tau) R(\tau\,|\,\lambda)\,d\tau \tag{5.2}$$

where $P_r(\delta_{\vec{r}}\omega|\tau)$ is the conditional probability distribution function of $\delta_{\vec{r}}\omega$ given τ. From Eq. (5.1) and letting $y(\tau) = (e^{-\lambda}+e^{-\mu\tau})/2$, we have,

$$P_r(\delta_{\vec{r}}\omega|\tau) = \frac{1}{y(\tau)} P_Z\left[\frac{\delta_{\vec{r}}\omega}{y(\tau)}\right] \tag{5.3}$$

where P_Z is the probability density function of Z. Note that when $r = L$, $\lambda = \tau = 0$, which implies $\delta_{\vec{r}}\omega|_{r=L} = Z$. Therefore, we obtain the result,

$$P_r(\delta_{\vec{r}}\omega) = \int_0^\infty \frac{1}{y(\tau)} P_L\left[\frac{\delta_{\vec{r}}\omega}{y(\tau)}\right] R(\tau\,|\,\lambda)\,d\tau\ . \tag{5.4}$$

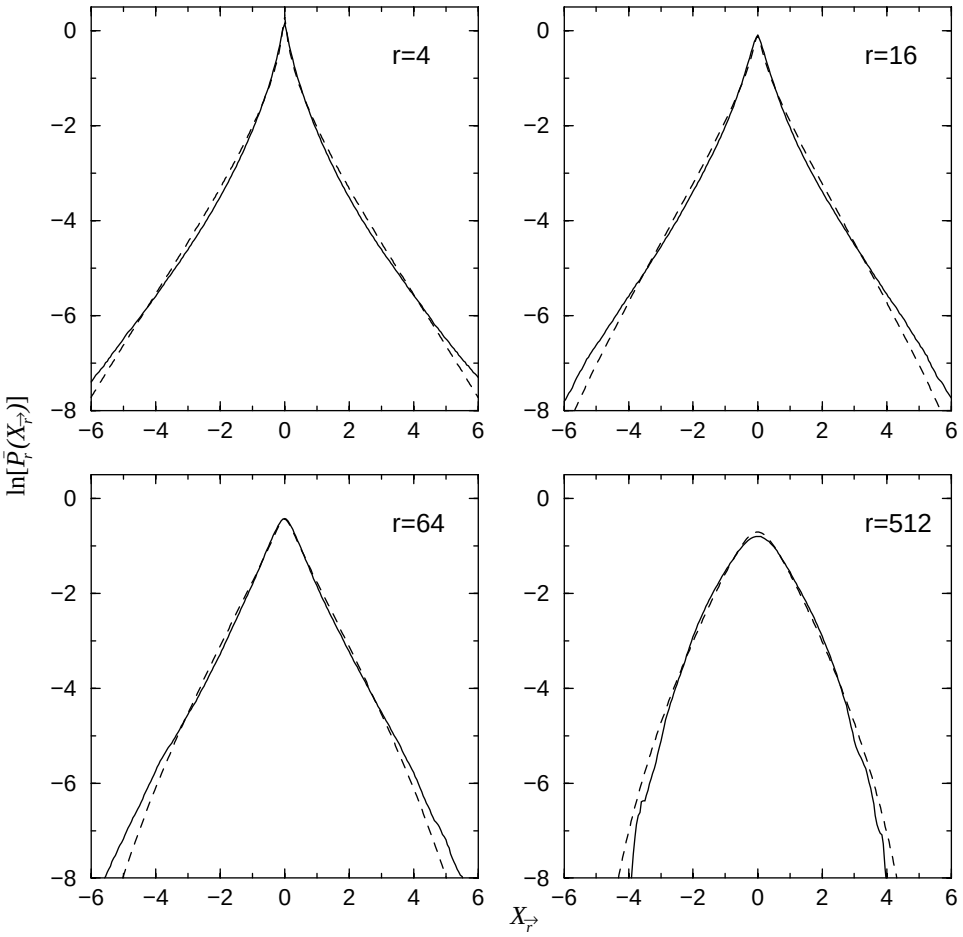

Figure 5.1: For $\mu = 0.1$, the probability distribution function $\bar{P}_r(X_{\vec{r}})$ of the standardized vorticity difference $X_{\vec{r}}$ obtained from direct numerical simulation (solid lines) and from Eq. (5.4) (dotted lines). The separating distance $\vec{r}$ is in the $\hat{x}$-direction and measured in the unit of grid size.

5.2 Comparison of Theory and Numerical Results

As customary in the study of intermittency problem, we consider the probability distribution function $\bar{P}_r(X_{\vec{r}})$ of the standardized vorticity difference $X_{\vec{r}}$, defined by Eq. (1.5). We first compute $\bar{P}_r(X_{\vec{r}})$ directly from the numerical solution of Eq. (1.2). The vorticity field $\omega(\vec{x}, t)$ from $t = 41$ to $t = 75$ at every 1 time unit is used in this computation. The separating distance $\vec{r}$ is taken to be in the $\hat{x}$-direction and is measured in the unit of grid size. For $\mu = 0.1$, the results for four different values of r are shown as solid lines in FIG. 5.1. It is clear that the shape of $\bar{P}_r(X_{\vec{r}})$ changes as r varies in the range of $4 \leq r \leq 512$, indicating the system is intermittent. $\bar{P}_r(X_{\vec{r}})$ develops

exponential tails (e.g., $r = 64$) and then stretched-exponential tails (e.g., $r = 4$) as r decreases. We note that $\bar{P}_r(X_{\vec{r}})$ for all $r \leq 4$ collapse onto each other, and similarly, all the $\bar{P}_r(X_{\vec{r}})$ with $r \geq 512$ have the same shape. Numerical results similar to those in FIG. 5.1 have also been obtained in Ref [13], theory for $\bar{P}_r(X_{\vec{r}})$ was not presented in Ref [13].

To apply the theoretical result Eq. (5.4), we first derive an expression for $R(\tau \,|\, \lambda)$. To this end, we approximate $G(h)$ as a quadratic function of h,

$$G(h) \approx a(h - \bar{h})^2 \ . \tag{5.5}$$

Using the relation Eq. (4.5) and the asymptotic form for $P(h \,|\, t)$, Eq. (2.15), we obtain

$$\begin{aligned} R(\tau \,|\, \lambda) &= \frac{\lambda}{2\tau^2} P(h = \frac{\lambda}{\tau} \,|\, \tau) \\ &\sim \frac{1}{2}\sqrt{\frac{a}{\pi\tau}} \left(\frac{\lambda}{\tau} - \bar{h}\right) e^{-\tau a \left(\frac{\lambda}{\tau} - \bar{h}\right)^2} \ . \end{aligned} \tag{5.6}$$

To compare the predictions by Eq. (5.4) with numerical results, the $G(h)$ for $\mu = 0.1$ shown in FIG. 3.1 is fitted to Eq. (5.5) in the vicinity of its minimum to obtain the parameters a and $\bar{h}$. This quadratic fit is a good approximation because the integral in Eq. (5.4) is dominated by the region where $R(\tau \,|\, \lambda)$ is large, which roughly corresponds to the region where $P(h \,|\, t)$ is maximum. FIG. 5.2 shows the $R(\tau \,|\, \lambda)$ for $\mu = 0.1$ obtained using the quadratic approximation Eq. (5.5). We then take P_L in Eq. (5.4) to be of the form $\exp(W)$ where W is an even sixth degree polynomial fitted to the numerically computed $\ln[P_r(\delta_{\vec{r}}\omega)]$ for $\vec{r} = 1024\hat{x}$ and $\mu = 0.1$. With $R(\tau \,|\, \lambda)$ and P_L obtained as described above, we compute $P_r(\delta_{\vec{r}}\omega)$, and thus $\bar{P}_r(X_{\vec{r}})$, for different values of r using Eq. (5.4). The results are plotted as dotted lines in FIG. 5.1. The theoretical predictions agree very well with the numerical results. We also find good agreements between our theory and numerical simulations when $\vec{r}$ is taken to be in the $\hat{y}$-direction. Similar results are obtained for the case $\mu = 0.2$.

5.3 Discussion

According to Eq. (5.4), $P_r(\delta_{\vec{r}}\omega)$ for a given r can be considered as a superposition of many different probability distribution functions, each obtained by rescaling $P_L(\delta_{\vec{r}}\omega)$ to a different width using

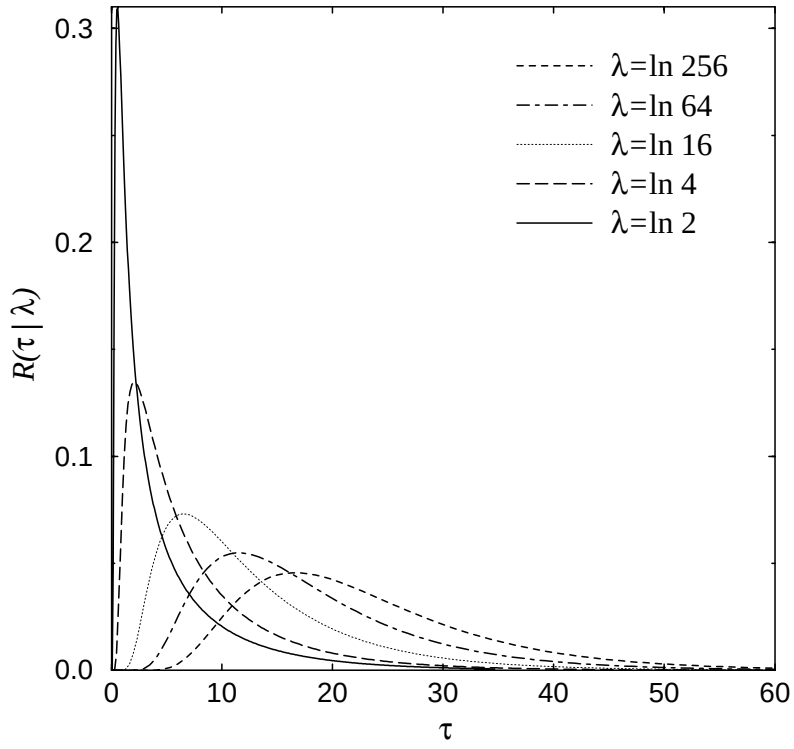

Figure 5.2: For $\mu = 0.1$, the conditional probability density function $R(\tau \,|\, \lambda)$ given by Eq. (5.6) ($a = 1.55$, $\bar{h} = 0.26$) for different values of λ.

$y(\tau)$. The amplitude of each component is then determined by the coefficient $R(\tau \,|\, \lambda)$. Since the statistics between two points separated by distance $r \sim L$ are uncorrelated, the distribution $P_L(\delta_{\vec{r}}\omega)$ is virtually the one-point probability distribution of the vorticity ω, which is not necessarily Gaussian and is closely related to the statistics of the source f_ω, as implied by the definition of Z. Hence, Eq. (5.4) relates the distribution of the vorticity difference to the one-point statistics of the source.

As can be seen in FIG. 5.2, $R(\tau \,|\, \lambda)$ has a very sharp peak when λ is small (r is large). Thus, only a small range of values of τ contributes to the integral Eq. (5.4). This gives the expected result that $P_r(\delta_{\vec{r}}\omega)$ has similar shape as $P_L(\delta_{\vec{r}}\omega)$ when r is large. As λ increases (r decreases), the width of $R(\tau \,|\, \lambda)$ increases. According to Eq. (5.4), $P_r(\delta_{\vec{r}}\omega)$ is now composed of a large number of rescaled $P_L(\delta_{\vec{r}}\omega)$ with a broad range of width. This gives rise to the broader-than-Gaussian tails in $P_r(\delta_{\vec{r}}\omega)$ for small r.

Like the anomalous scaling of the vorticity structure functions, the dependence of the shape of $P_r(\delta_{\vec{r}}\omega)$ on r is a result of the presence of drag and the non-uniform stretching of fluid elements. If $h = \bar{h}$ for all fluid trajectories, then $R(\tau \,|\, \lambda) = \delta(\tau - \lambda/\bar{h})$, and from Eq. (5.4), $P_r(\delta_{\vec{r}}\omega)$ has the same form for all r, indicating a self-similar flow. On the other hand, if $\mu = 0$, $y(\tau)$ becomes independent of τ, which also implies $P_r(\delta_{\vec{r}}\omega)$ is independent of r. In both situations, $P_r(\delta_{\vec{r}}\omega)$ will have the same shape as $P_L(\delta_{\vec{r}}\omega)$.

We remark that while the width of the distribution $P_r(\delta_{\vec{r}}\omega)$ in Eq. (5.4) depends precisely on the choice of the value for the multiplicative constant on the right hand side of Eq. (5.1), our results for $\bar{P}_r(X_{\vec{r}})$ is independent of the value of such constant

Chapter 6 Multifractal Formulation

6.1 Theory

The local viscous energy dissipation rate per unit mass ε and its global average value $\langle\varepsilon\rangle$ play important roles in the phenomenology of three-dimensional turbulence [27]. It is now well known that ε shows intermittent spatial fluctuations which can be described by the multifractal formulation [28]. Using the measure $p'(r) = \mathcal{E}_r/\mathcal{E}$, where $\mathcal{E}_r$ is the total dissipation in a volume of linear dimension r and $\mathcal{E}$ is the total dissipation in the whole domain, the Rényi dimension spectrum D_q and the singularity spectrum $f(\alpha)$ have been measured experimentally [29, 30].

Intermittency in three-dimensional turbulence also manifests itself as anomalous scaling in the velocity structure functions $S'_{3q}(r)$ defined as

$$S'_{3q}(r) = \langle(\delta_{\vec{r}}v)^{3q}\rangle \sim r^{\zeta'_{3q}} \ , \tag{6.1}$$

where v is the component of the velocity vector in the direction of $\vec{r}$ and $\delta_{\vec{r}}v = v(\vec{x}+\vec{r}) - v(\vec{x})$. From Kolmogorov's hypotheses in his 1941 paper [31], which ignore the intermittency of ε, one arrives at the result $\zeta'_{3q} = q$. Experiments show that ζ'_{3q} is a nonlinear function of q. This anomalous scaling of $S'_{3q}(r)$ is believed to be related to the intermittency of ε. Kolmogorov's 'refined similarity hypothesis' in his 1962 paper [32] gives the connection between intermittency in velocity difference and intermittency in ε. The refined similarity hypothesis states that at very high Reynolds numbers, there is an inertial range of r in which the conditional moments of $\delta_{\vec{r}}v$ scales as follows

$$\langle(\delta_{\vec{r}}v)^q \,\big|\, \varepsilon_r\rangle \sim (r\varepsilon_r)^{q/3} \ , \tag{6.2}$$

where ε_r is the average of ε over a volume of linear dimension r. Eq. (6.2) implies $\langle(\delta_{\vec{r}}v)^q\rangle \sim \langle(r\varepsilon_r)^{q/3}\rangle$ which gives the following relation between the D_q based on $p'(r)$ and ζ'_{3q},

$$D_q = 3 + \frac{\zeta'_{3q} - q\zeta'_3}{q-1} \ . \tag{6.3}$$

Kolmogorov's fourth-fifths law gives $\zeta'_3 = 1$ exactly [28]. Eq. (6.3) can also be derived [30] from

the relation

$$\varepsilon_r \sim \frac{(\delta_{\vec{r}} v)^3}{r} \ . \tag{6.4}$$

We note that Eq. (6.2) follows from Eq. (6.4). As shown below, there is a relation analogous to Eq. (6.3) for the enstrophy cascade of two-dimensional turbulence with drag.

For the enstrophy cascade regime in two-dimensional turbulence, a central quantity to the phenomenology [8] in this regime is the viscous enstrophy dissipation η given by Eq. (1.8), and the relevant measure is $p_i(\epsilon)$ defined in Eq. (1.9). We have already seen in Chapter 4 that in the presence of drag, the vorticity structure functions scale anomalously with scaling exponents ζ_{2q} given by Eq. (4.6). We now derive a relation between ζ_{2q} and the D_q based on $p_i(\epsilon)$.

Consider the following quantity

$$I_1(q,\epsilon) = \sum_i p_i^q(\epsilon) \tag{6.5}$$

which by the definition of D_q, Eq. (1.10), scales like

$$I_1(q,\epsilon) \sim \epsilon^{(q-1)D_q} \tag{6.6}$$

for some range of ϵ. Assume there exists a scaling range extending from the system scale $L \sim k_f^{-1}$ down to the dissipative scale $r_d \sim k_d^{-1}$ such that both the scaling relations Eq. (1.4) and Eq. (6.6) hold. At the dissipative scale, due to the action of viscosity, the vorticity field ω becomes smooth, thus we have the following relations,

$$\int_{\mathcal{R}(r_d)} |\nabla\omega|^2 d\vec{x} \ \sim \ r_d^2 \, |\nabla\omega(\vec{x})|^2 \ , \qquad \vec{x} \in \mathcal{R}(r_d) \tag{6.7}$$

$$|\nabla\omega| \ \sim \ \frac{|\delta_{\vec{r}}\omega|}{r_d} \ , \qquad |\vec{r}| = r_d \ . \tag{6.8}$$

Then by putting $\epsilon = r_d$ in Eq. (1.9) and let $|\vec{r}| = r_d$ and $\vec{x}_i \in \mathcal{R}_i(r_d)$, we get

$$p_i(r_d) \sim \frac{|\delta_{\vec{r}}\omega(\vec{x}_i)|^2}{(r_d)^{-2} \int_{\mathcal{R}} |\delta_{\vec{r}}\omega|^2 \, d\vec{x}} \ . \tag{6.9}$$

Substituting Eq. (6.9) in Eq. (6.5), we obtain the scaling of $I_1(q,\epsilon)$,

$$\begin{aligned} I_1(q,r_d) &\sim \frac{\sum_i |\delta_{\vec{r}}\omega(\vec{x}_i)|^{2q}}{\frac{1}{(r_d)^{2q}}\left(\int_{\mathcal{R}} |\delta_{\vec{r}}\omega|^2\, d\vec{x}\right)^q} \\ &\sim \frac{\left(\frac{L}{r_d}\right)^2 \langle |\delta_{\vec{r}}\omega|^{2q}\rangle}{\left(\frac{L}{r_d}\right)^{2q} \langle |\delta_{\vec{r}}\omega|^2\rangle^q} \\ &\sim (r_d)^{2q-2+\zeta_{2q}-q\zeta_2}\ . \end{aligned} \tag{6.10}$$

Comparing Eq. (6.6) to Eq. (6.10), we get the principal result of this section,

$$D_q = 2 + \frac{\zeta_{2q} - q\zeta_2}{q-1} \tag{6.11}$$

which can be regarded as analogous to Eq. (6.3).

We mention that Eq. (6.3) can be derived in an analogous manner using Eq. (6.4). From Eq. (6.11), in two-dimensional turbulence, the measure p_i is multifractal when the vorticity structure functions exhibit anomalous scaling. Hence, in the presence of drag, we expect the measure based on the squared vorticity gradient $|\nabla\omega|^2$ to show multifractal structures.

6.2 Comparison of Theory and Numerical Results

The multifractal structure of $|\nabla\omega|^2$ is most readily visualized in snapshots of $|\nabla\omega|^2$ from our simulations. Since $|\nabla\omega|^2$ grows at widely varying exponential rates, only a few points would be visible if $|\nabla\omega|^2$ was plotted directly using a linear scale. Therefore, we plot the following quantity instead [24],

$$\mathcal{M}(\vec{x}) = \frac{\sum_{\vec{x}_i\in\Lambda_{\vec{x}}} |\nabla\omega(\vec{x}_i)|^2}{\sum_i |\nabla\omega(\vec{x}_i)|^2}\ , \tag{6.12}$$

where the set $\Lambda_{\vec{x}}$ contains those lattice points $\vec{x}_i$ for which $|\nabla\omega(\vec{x}_i)|^2 \le |\nabla\omega(\vec{x})|^2$, and we sum over all lattice points in the denominator. By definition, $0 \le \mathcal{M}(\vec{x}) \le 1$. FIG. 6.1 shows the results for $\mu = 0.1$ and $\mu = 0.2$. Filament structures can clearly be seen for both cases, showing that the measure p_i concentrates in a very small area. This is particularly clear in the case $\mu = 0.2$.

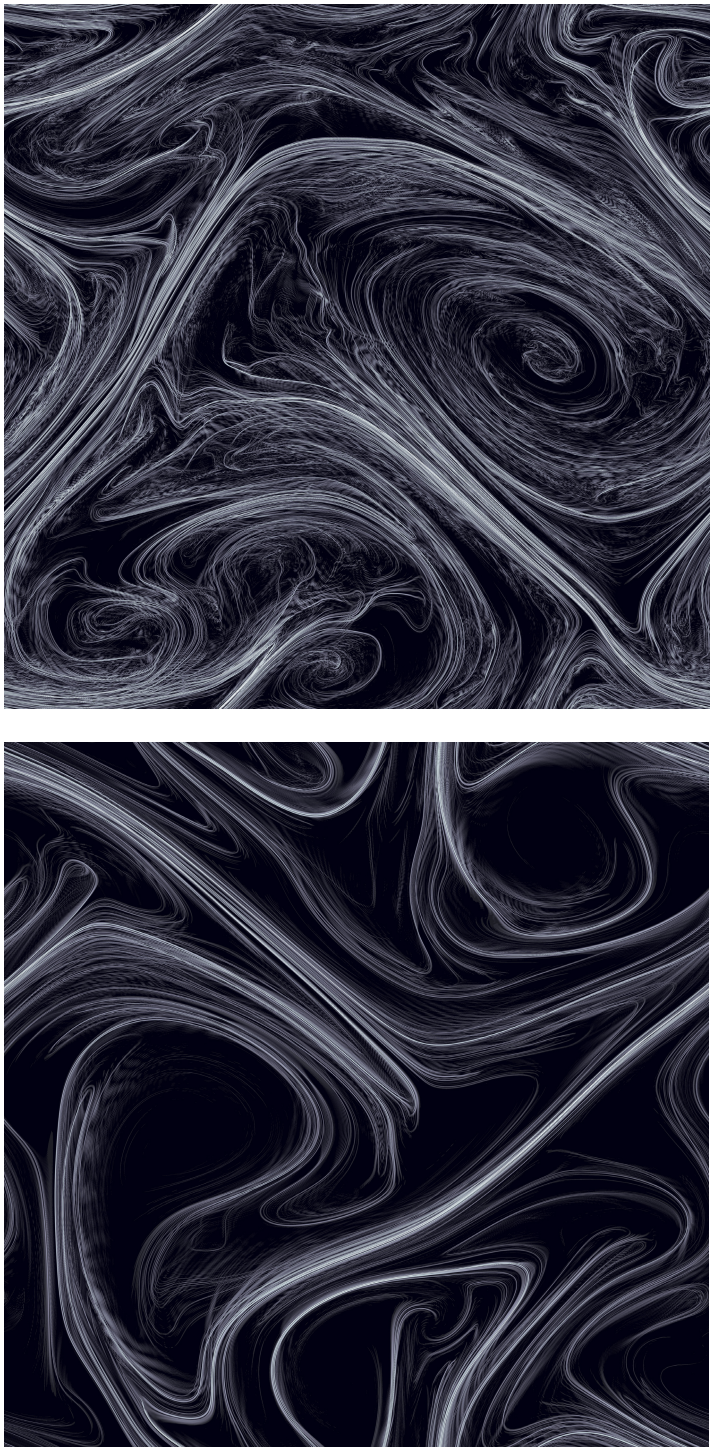

Figure 6.1: Snapshots of the scaled squared vorticity gradient $|\nabla\omega|^2$ at $t = 61$ for the case $\mu = 0.1$ (upper) and at $t = 65$ for the case $\mu = 0.2$ (lower). Light areas are regions of large values, and dark areas are regions of small values.

To quantify the multifractal nature of p_i, we now calculate its Rényi dimension spectrum D_q. We employ the box-counting method to estimate D_q. Using box size ϵ/L ranging from 2^{-12} to 2^{-1}, we compute the instantaneous $I_1(q,\epsilon)$ from $t = 41$ to $t = 75$ at every 1 time unit using the numerical solution of Eq. (1.2). For $q \neq 1$, we then make log-log plot of the time-average of $[I_1/(q-1)]$ versus ϵ/L. For $q = 1$, we take the limit $q \to 1$ in Eq. (6.6) to obtain $I_2(\epsilon) \sim \epsilon^{D_1}$, where

$$I_2(\epsilon) = \sum_i p_i(\epsilon) \log_2[p_i(\epsilon)] \tag{6.13}$$

and for $q = 1$ in FIGS. 6.2(a) and 6.3(a), the time average of $I_2(\epsilon)$ is plotted against $\log_2(\epsilon/L)$. According to Eq. (6.6), these plots will show a linear region with slope equals D_q. FIGS. 6.2(a) and 6.3(a) are the resulting plots for the cases $\mu = 0.1$ and $\mu = 0.2$ respectively, each showing several typical values of q. All curves show slightly undulating behavior which introduces uncertainties in the determination of D_q. The estimated D_q at different values of q are shown as circles with error bars in FIGS. 6.2(b) and 6.3(b). The error bars correspond to the variability of the D_q observed at different moments in time. The dotted lines in the figures are fourth degree polynomials fitted to the circles. We also compute D_q using Eq. (6.11). To this end, we fit the curves of ζ_{2q}/ζ_2 versus q in FIG. 4.1(b) and FIG. 4.2(b) with the following fourth degree polynomial,

$$\frac{\zeta_{2q}}{\zeta_2} = q\left[1 + \sum_{n=1}^{3} a_n (q-1)^n\right] \ . \tag{6.14}$$

By Eq. (6.11), D_q is then given by

$$D_q = 2 + \zeta_2 \sum_{n=1}^{3} a_n q (q-1)^{n-1} \ . \tag{6.15}$$

In FIGS. 6.2(b) and 6.3(b), we plot Eq. (6.15) using ζ_{2q} obtained from numerical simulations, as well as ζ_{2q} calculated from our theory. The results are shown as solid lines labeled with squares and diamonds, respectively. Despite the fact that there are discrepancies between the D_q obtained by the various methods, they all show the same trend and clearly indicates that p_i is multifractal (*i.e.*, D_q varies with q).

We now generate the singularity spectrum $f(\alpha)$ by Legendre transforming the D_q curves

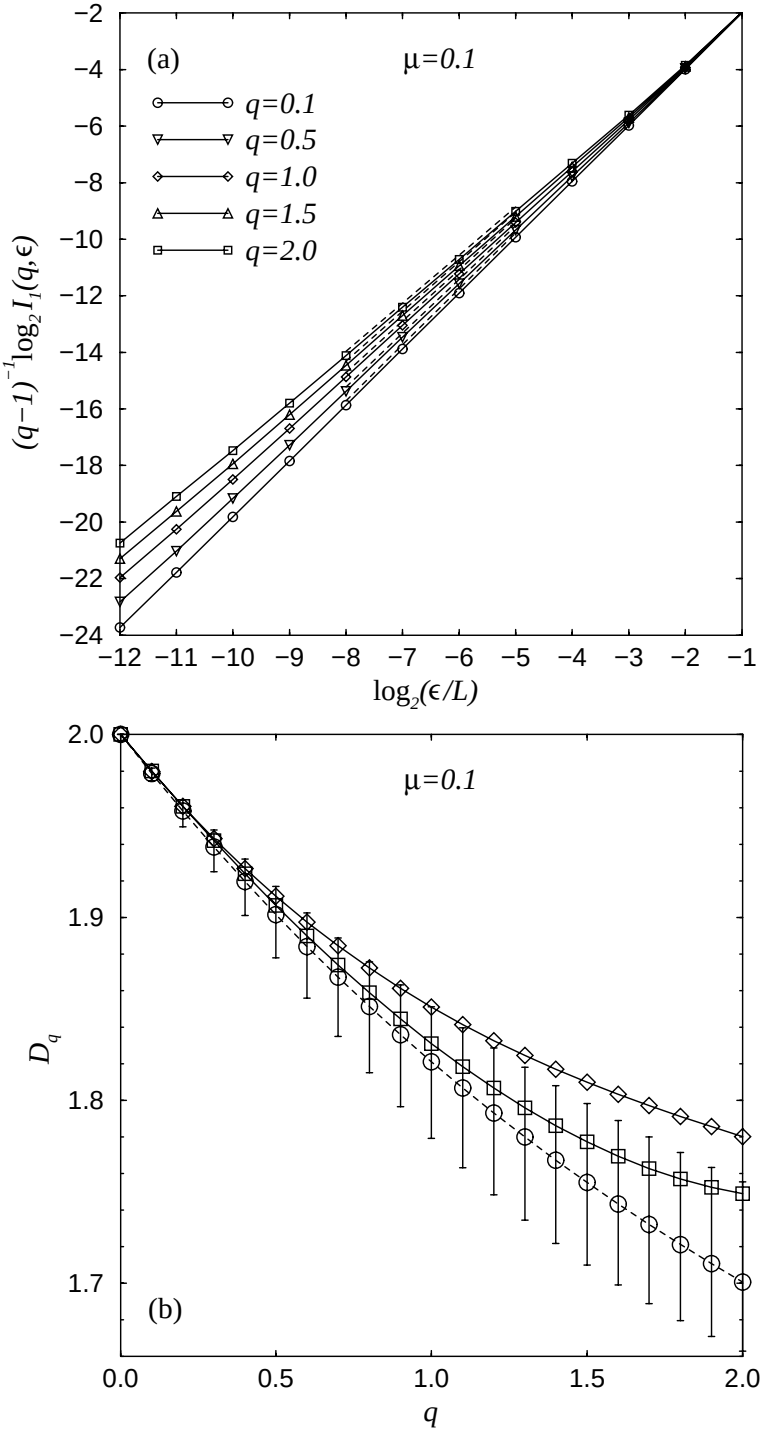

Figure 6.2: For the case of $\mu = 0.1$: (a) $I_1(q, \epsilon)$ for q between 0.1 and 2.0 ($I_2(\epsilon)$ is plotted for $q = 1.0$). The dotted lines are linear fits in the scaling region. (b) D_q computed using numerical solution of Eq. (1.2) (circle with error bar) and its fourth degree polynomial fit (dotted line). D_q predicted by the theory Eq. (6.11) when ζ_{2q} obtained from numerical simulations are used (square) and when ζ_{2q} calculated from Eq. (4.6) are used (diamond).

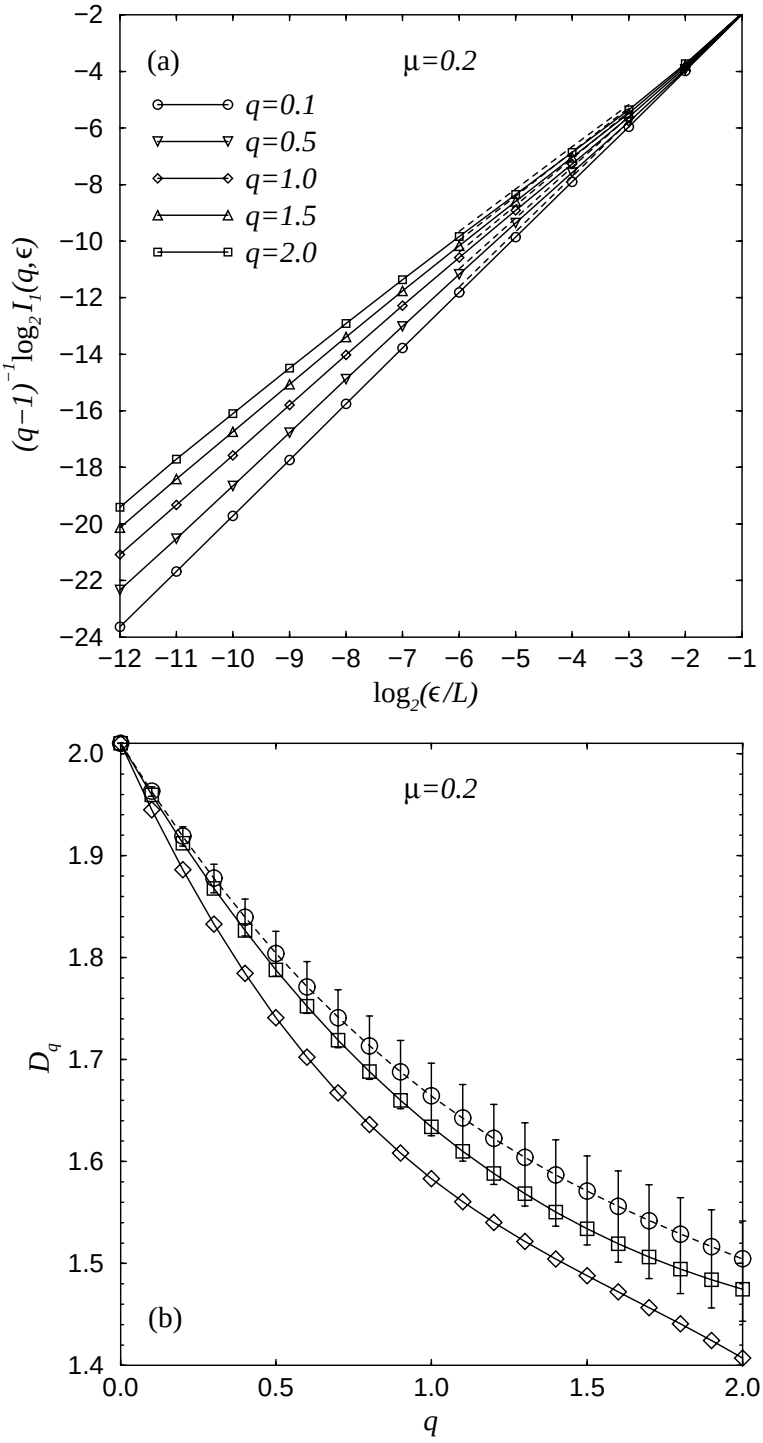

Figure 6.3: For the case of $\mu = 0.2$: (a) $I_1(q, \epsilon)$ for q between 0.1 and 2.0 ($I_2(\epsilon)$ is plotted for $q = 1.0$). The dotted lines are linear fits in the scaling region. (b) D_q computed using numerical solution of Eq. (1.2) (circle with error bar) and its fourth degree polynomial fit (dotted line). D_q predicted by the theory Eq. (6.11) when ζ_{2q} obtained from numerical simulations are used (square) and when ζ_{2q} calculated from Eq. (4.6) are used (diamond).

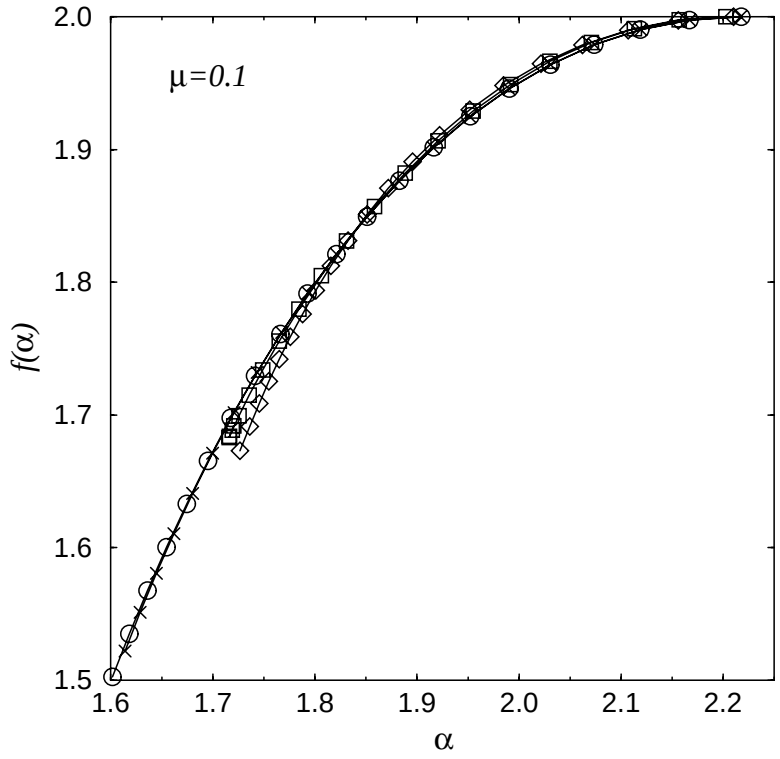

Figure 6.4: For the case of $\mu = 0.1$: The $f(\alpha)$ curves generated by Legendre transforming the D_q curves in FIG. 6.2(b) with the corresponding labels (circle, square and diamond). $f(\bar{\alpha})$ at different values of $\bar{\alpha}$ obtained by the canonical method is shown as well (cross).

shown in FIGS. 6.2(b) and 6.3(b). In particular, for each value of q, we have [17]

$$\alpha(q) = \frac{d}{dq}\left[(q-1)D_q\right] , \tag{6.16}$$

$$f[\alpha(q)] = \alpha q - (q-1)D_q . \tag{6.17}$$

In the absence of intermittency D_q is independent of q and $f(\alpha)$ is defined only at $\alpha = D_q$. Thus the consistent determination of $f(\alpha)$ over some range of α indicates intermittency. FIG. 6.4 and FIG. 6.5 show the $f(\alpha)$ obtained for $\mu = 0.1$ and $\mu = 0.2$ respectively using the D_q obtained by the three methods in FIG. 6.2(b) and 6.3(b) (circle, square and diamond symbols). The results for $f(\alpha)$ are seen to agree very well with each other in spite of the difference between the D_q determinations. Thus, we find that $f(\alpha)$ gives a more consistent measure of intermittency across different methods of determination than does D_q. We believe that the disagreement seen in FIGS. 6.2(b) and 6.3(b) between the different methods for determining D_q is not significant in view the limited amount of

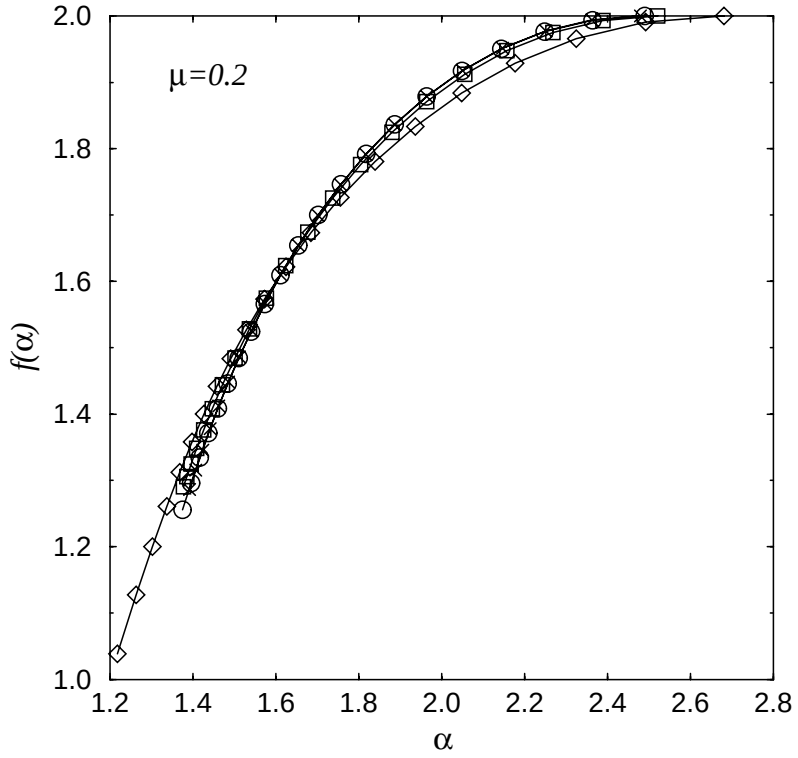

Figure 6.5: For the case of $\mu = 0.2$: The $f(\alpha)$ curves generated by Legendre transforming the D_q curves in FIG. 6.3(b) with the corresponding labels (circle, square and diamond). $f(\bar{\alpha})$ at different values of $\bar{\alpha}$ obtained by the canonical method is shown as well (cross).

scaling range available.

We can also determine $f(\alpha)$ directly from the numerical solution of Eq. (1.2). Following Ref. [29], we use the canonical method developed in Ref. [33] to determine $f(\alpha)$. Accordingly, we construct the normalized q^{th} order measures $m_i(q,\epsilon)$ in box $\mathcal{R}_i(\epsilon)$ as follow,

$$m_i(q,\epsilon) = \frac{p_i^q(\epsilon)}{\sum_j p_j^q(\epsilon)} \ . \tag{6.18}$$

Then, the mean singularity index $\bar{\alpha}$ and the corresponding $f(\bar{\alpha})$ is given by

$$\bar{\alpha}(q) = \sum_i m_i \alpha_i = \lim_{\epsilon\to 0}\lim_{\nu\to 0} \frac{\sum_i m_i \log p_i}{\log \epsilon} \ , \tag{6.19}$$

$$f[\bar{\alpha}(q)] = \lim_{\epsilon\to 0}\lim_{\nu\to 0} \frac{\sum_i m_i \log m_i}{\log \epsilon} \ . \tag{6.20}$$

One of the advantages of the canonical method is the absence of finite-size effect due to logarithmic prefactors [29]. To estimate $\bar{\alpha}$, we plot the time average of the quantity $\sum_i m_i \log_2 p_i$ versus

$\log_2(\epsilon/L)$ and measure the slopes in the scaling region. Similarly, when we plot the time average of $\sum_i m_i \log_2 m_i$ versus $\log_2(\epsilon/L)$, the slopes in the scaling range give the values of $f(\bar{\alpha})$. For the case $q = 1$, $\bar{\alpha}(1) = f[\bar{\alpha}(1)]$ is obtained by measuring the slope of the curve of the time-averaged $I_2(1, \epsilon)$ versus $\log_2(\epsilon/L)$. The values of $f(\bar{\alpha})$ at different values of $\bar{\alpha}$ obtained by this scheme are shown as crosses in FIG. 6.4 and FIG. 6.5 for $\mu = 0.1$ and $\mu = 0.2$ respectively. They are in excellent agreement with the $f(\alpha)$ generated by Legendre transforming the D_q curve obtained from the numerical solution of Eq. (1.2).

6.3 Discussion

Kolmogorov introduced the refined similarity hypothesis (RSH) Eq. (6.2) to take into account the spatial fluctuations of ε in three-dimensional turbulence. The relation Eq. (6.3) is a direct consequence of the RSH. In two-dimensional turbulence, the relevant quantity is the local rate of viscous enstrophy dissipation η. We have already seen that the measure p_i is multifractal in the presence of drag, indicating the intermittent nature of η. Following Kolmogorov's ideas, we consider the average of η over an area $\mathcal{R}(r)$ of linear dimension r:

$$\eta_r = \frac{\nu}{r^2} \int_{\mathcal{R}(r)} |\nabla\omega|^2 \, d\vec{x} \; . \tag{6.21}$$

Analogous to the Kolmogorov's RSH, we propose that at high Reynolds number, there is an inertial range of r in which

$$\langle |\delta_{\vec{r}}\omega|^{2q} \, \big| \, \eta_r \rangle = C_{2q} (r^{\zeta_2} \eta_r)^q \tag{6.22}$$

where C_{2q} are constants. Eq. (6.22) implies $\langle |\delta_{\vec{r}}\omega|^{2q} \rangle \sim \langle (\eta_r)^q \rangle r^{q\zeta_2}$ and hence $\langle (\eta_r)^q \rangle \sim r^{\gamma_q}$ with

$$\gamma_q = \zeta_{2q} - q\zeta_2 \; . \tag{6.23}$$

An expression analogous to Eq. (6.23) has been proven for Kraichnan's model of passive scalar advection [34, 35]. We note that Eq. (6.22) follows if

$$\eta_r \sim \frac{(\delta_{\vec{r}}\omega)^2}{r^{\zeta_2}} \tag{6.24}$$

which is the two-dimensional counterpart of Eq. (6.4). It is straightforward to show that the hypothesis Eq. (6.22) implies Eq. (6.11). Denoting η_r in box $\mathcal{R}_i(r)$ by $\eta_r^{(i)}$, we have

$$p_i(r) = \frac{r^2}{L^2} \frac{\eta_r^{(i)}}{\langle \eta \rangle} \ . \tag{6.25}$$

Since $\sum_i [\eta_r^{(i)}]^q \sim r^{-2} \langle (\eta_r)^q \rangle$, we get $I(q,r) \sim r^{2q-2+\gamma_q}$, from which Eq. (6.11) immediately follows.

Finally, we remark that if the measure p_i is defined with a parameter n as follow [24],

$$p_i(\epsilon, n) = \frac{\int_{\mathcal{R}_i(\epsilon)} |\nabla \omega|^n \, d\vec{x}}{\int_{\mathcal{R}} |\nabla \omega|^n \, d\vec{x}} \ , \tag{6.26}$$

then the corresponding formula for the D_q based on this measure is

$$D_q = 2 + \frac{\zeta_{nq} - q\zeta_n}{q-1} \ . \tag{6.27}$$

Chapter 7 Conclusion

We have studied the enstrophy cascade regime of two-dimensional turbulence with linear drag. A previous theory relating the power law exponent of the energy wavenumber spectrum to the distribution of finite-time Lyapunov exponents $P(h\,|\,t)$ is verified by direct numerical computation using a 4096×4096 lattice. We also calculate the vorticity structure functions numerically and show that they exhibit anomalous scaling in the presence of drag. The values of the structure function scaling exponents ζ_{2q} are measured and found to agree with the prediction by a previous theory which relates ζ_{2q} to $P(h\,|\,t)$. We then compute the probability distribution function $\bar{P}_r(X_{\vec{r}})$ of the standardized vorticity difference $X_{\vec{r}}$ and find that $\bar{P}_r(X_{\vec{r}})$ develops exponential and stretched-exponential tails at small values of r. We derive a theoretical expression for $\bar{P}_r(X_{\vec{r}})$, which gives predictions that agree well with the numerical results for a wide range of r. A measure based on the local viscous enstrophy dissipation rate η is studied in terms of its Rényi dimension spectrum D_q and singularity spectrum $f(\alpha)$, and is found to be multifractal. The intermittency in η is connected to the intermittency in vorticity difference by a two-dimensional analog of the refined similarity hypothesis, and we derive a formula that relates D_q to ζ_{2q}.

BIBLIOGRAPHY

[1] M. C. Kelley and E. Ott, J. Geophys. Res. **83**, 4369 (1978).

[2] G. D. Nastrom and K. S. Gage, J. Atmos. Sci. **42**, 950 (1985).

[3] H. Kellay, X. L. Wu, and W. I. Goldburg, Phys. Rev. Lett. **80**, 277 (1998).

[4] M. A. Rutgers, Phys. Rev. Lett. **81**, 2244 (1998).

[5] J. Paret, M.-C. Jullien, and P. Tabeling, Phys. Rev. Lett. **83**, 3418 (1999).

[6] C. N. Baroud, B. B. Plapp, Z.-S. She, and H. L. Swinney, Phys. Rev. Lett. **88**, 114501 (2002).

[7] H. Kellay and W. I. Goldburg, Rep. Prog. Phys. **65**, 845 (2002).

[8] R. H. Kraichnan, Phys. Fluids **10**, 1417 (1967).

[9] R. H. Kraichnan, J. Fluid Mech. **47**, 525 (1971).

[10] K. Nam, T. M. Antonsen, Jr., P. N. Guzdar, and E. Ott, Physica A **288**, 265 (2000).

[11] K. Nam, E. Ott, T. M. Antonsen, Jr., and P. N. Guzdar, Phys. Rev. Lett. **84**, 5134 (2000).

[12] D. Bernard, Europhys. Lett. **50**, 333 (2000).

[13] G. Boffetta, A. Celani, S. Musacchio, and M. Vergassola, Phys. Rev. E **66**, 026304 (2002).

[14] A. Rényi, *Probability Theory* (North-Holland, Amsterdam, 1970).

[15] P. Grassberger, Phys. Lett. A **97**, 227 (1983).

[16] H. G. E. Hentschel and I. Procaccia, Phyisca D **8**, 435 (1983).

[17] T. C. Halsey, M. H. Jensen, L. P. Kadanoff, I. Procaccia, and B. I. Shraiman, Phys. Rev. A **33**, 1141 (1986).

[18] E. Ott, *Chaos in Dynamical Systems* (Cambridge University Press, 2002), 2nd ed.

[19] Z. Neufeld, C. López, E. Hernández-García, and T. Tél, Phys. Rev. E **61**, 3857 (2000).

[20] G.-C. Yuan, K. Nam, T. M. Antonsen, Jr., E. Ott, and P. N. Guzdar, Chaos **10**, 39 (2000).

[21] T. M. Antonsen, Jr., Z. Fan, E. Ott, and E. Garcia-Lopez, Phys. Fluids **8**, 3094 (1996).

[22] K. Nam, T. M. Antonsen, Jr., P. N. Guzdar, and E. Ott, Phys. Rev. Lett. **83**, 3426 (1999).

[23] E. Ott and T. M. Antonsen, Jr., Phys. Rev. A **39**, 3660 (1989).

[24] F. Városi, T. M. Antonsen, Jr., and E. Ott, Phys. Fluids A **3**, 1017 (1991).

[25] M. Chertkov, Phys. Fulids **10**, 3017 (1998).

[26] C. Reyl, T. M. Antonsen, Jr., and E. Ott, Physica D **111**, 202 (1998).

[27] G. Stolovitzly and K. R. Sreenivasan, Rev. Mod. Phys. **66**, 229 (1994).

[28] U. Frisch, *Turbulence* (Cambridge University Press, 1995).

[29] A. B. Chhabra, C. Meneveau, R. V. Jensen, and K. R. Sreenivasan, Phys. Rev. A **40**, 5284 (1989).

[30] C. Meneveau and K. R. Sreenivasan, J. Fluid Mech. **224**, 429 (1991).

[31] A. N. Kolmogorov, Dokl. Akad. Nauk SSSR **30**, 301 (1941).

[32] A. N. Kolmogorov, J. Fluid Mech. **13**, 82 (1962).

[33] A. Chhabra and R. V. Jensen, Phys. Rev. Lett. **62**, 1327 (1989).

[34] R. H. Kraichnan, V. Yakhot, and S. Chen, Phys. Rev. Lett. **75**, 240 (1995).

[35] M. Chertkov and G. Falkovich, Phys. Rev. Lett. **76**, 2706 (1996).